HHS Public Access

Author manuscript

Hear Res. Author manuscript; available in PMC 2024 August 01.

Published in final edited form as:

Hear Res. 2023 August ; 435: 108822. doi:10.1016/j.heares.2023.108822.

Group I metabotropic glutamate receptor-triggered temporally patterned action potential-dependent spontaneous synaptic transmission in mouse MNTB neurons

Huimei Wang[1,#], **Kang Peng**[1,#], **Rebecca J. Curry**[1,2], **Dong Li**[1], **Yuan Wang**[3], **Xiaoyu Wang**[3], **Yong Lu, Ph.D.**[1,2,*]

[1]Hearing Research Group, Department of Anatomy and Neurobiology, College of Medicine Northeast Ohio Medical University, Rootstown, OH 44272, USA

[2]School of Biomedical Sciences, Kent State University, Kent, OH 44240, USA

[3]Department of Biomedical Science, Program in Neuroscience, Florida State University College of Medicine, Tallahassee, FL 32306, USA

Abstract

Rhythmic action potentials (AP) are generated via intrinsic ionic mechanisms in pacemaking neurons, producing synaptic responses of regular inter-event intervals (IEIs) in their targets. In auditory processing, evoked temporally patterned activities are induced when neural responses timely lock to a certain phase of the sound stimuli. Spontaneous spike activity, however, is a stochastic process, rendering the prediction of the exact timing of the next event completely based on probability. Furthermore, neuromodulation mediated by metabotropic glutamate receptors (mGluRs) is not commonly associated with patterned neural activities. Here, we report an intriguing phenomenon. In a subpopulation of medial nucleus of the trapezoid body (MNTB) neurons recorded under whole-cell voltage-clamp mode in acute mouse brain slices, temporally

[*]**Correspondence to**: Yong Lu, Ph.D., Telephone: 330-325-6656, Facsimile: 330-325-5916, ylu@neomed.edu.
[#]These two authors contributed equally.

Author Contributions

YL conceived and supervised the study. HW, KP, RC, DL, YW, XW, and YL designed the experiments, performed the experiments, and analyzed data. All authors participated in writing the paper. All authors have approved the final version of the manuscript and agree to be accountable for all aspects of the work in ensuring that questions related to the accuracy or integrity of any part of the work are appropriately investigated and resolved. All persons designated as authors qualify for authorship, and all those who qualify for authorship are listed.

Conflict of Interest Statement

The authors declare no competing financial interests.

Ethics Statement

The animal study was reviewed and approved by the Institutional Animal Care and Use Committee of NEOMED and Florida State University.

Author Statement

YL conceived and supervised the study. HW, KP, RC, DL, YW, XW, and YL designed the experiments, performed the experiments, and analyzed data. All authors participated in writing the paper. All authors have approved the final version of the manuscript and agree to be accountable for all aspects of the work in ensuring that questions related to the accuracy or integrity of any part of the work are appropriately investigated and resolved. All persons designated as authors qualify for authorship, and all those who qualify for authorship are listed.

patterned AP-dependent glycinergic sIPSCs and glutamatergic sEPSCs were elicited by activation of group I mGluRs with 3,5-DHPG (200 μM). Auto-correlation analyses revealed rhythmogenesis in these synaptic responses. Knockout of mGluR5 largely eliminated the effects of 3,5-DHPG. Cell-attached recordings showed temporally patterned spikes evoked by 3,5-DHPG in potential presynaptic VNTB cells for synaptic inhibition onto MNTB. The amplitudes of sEPSCs enhanced by 3,5-DHPG were larger than quantal size but smaller than spike-driven calyceal inputs, suggesting that non-calyceal inputs to MNTB might be responsible for the temporally patterned sEPSCs. Finally, immunocytochemical studies identified expression and localization of mGluR5 and mGluR1 in the VNTB-MNTB inhibitory pathway. Our results imply a potential central mechanism underlying the generation of patterned spontaneous spike activity in the brainstem sound localization circuit.

Keywords

EPSC; IPSC; metabotropic glutamate receptor; temporally patterned synaptic activity; spontaneous transmitter release; medial nucleus of the trapezoid body

1. Introduction

Rhythmic action potentials (AP) exist in life-sustaining centers in the nervous system that control heartbeat, respiration, and locomotion (review in Moore et al., 2014; Del Negro et al., 2018) including newborn's crying (Wei et al., 2022). Neurons in the brainstem reticular formation, where the central control for respiration and heartbeat resides, generate rhythmic spike firing essential for survival during early development. Such rhythmic spike activities maintain for the life span of the organisms. Regulation of neuronal properties and top-down control are the underlying mechanisms of such rhythmogenesis (review in Shamir, 2019). The targets of the rhythmically firing neurons, consequently, receive temporally patterned synchronized neurotransmitter release and thus respond with synaptic activities of regular inter-event intervals (IEIs), to maintain a relatively constant heartbeat and regular breathing. In sensory processing, such patterned activities exist as a specialized neuronal property, such as phase-locking of auditory neurons for precise temporal coding (review in Heil and Peterson, 2017). Alternatively, such temporally patterned spike activities can be induced by artificially manipulating the sensory stimuli in such a way that neural responses lock to the timing of the stimuli with regular IEIs. Interestingly, the rhythm in heartbeat and respiration exerts influences on the sensitivity of somatosensory perception (Grund et al., 2022).

Unlike periodic stimulus-evoked transmitter release, generation of action potential (AP)-dependent spontaneous transmitter release in CNS neurons is considered a stochastic process, with the timing of synaptic events being governed by probability (review in Kavalali, 2015). The distribution of the IEIs of such events is without any periodicity (Cohen et al., 1974). In the auditory system, such spontaneous random firing is re-organized to be orderly (e.g., phase-locking) when a low frequency sound stimulus is given, causing neurons to fire APs at a certain phase of the sinusoidal waveform of the sound (review in Heil and Peterson, 2017). The synaptic responses underlying the generation of the timely precise spikes are mediated primarily by fast ionotropic glutamate receptors (review in

Leão, 2019). In contrast, metabotropic glutamate receptors (mGluRs), as subfamily 3 G-protein-coupled receptors (GPCRs), typically mediate much slower-onset and longer-lasting modulatory effects on neuronal properties (review in Niswender and Conn, 2010). Thus, mGluR-mediated responses are usually not associated with fast cycle-to-cycle modulation that underlies temporally patterned neural activities.

However, a number of studies have shown unconventional actions of some GPCRs on neuronal spiking activities. The slow responses of GPCRs could constrain the ability of neural networks in generating inputs at certain frequency, forming rhythmic oscillations. In a number of neural pathways such as the motor circuits in the spinal cord and brainstem, activation of mGluRs results in bursting AP firing and rhythmic neural activities (review in Nistri et al., 2006), and modulates rhythmic motor patterns (review in El Manira et al., 2002). Activation of group I mGluRs (mGluR I, including mGluR1 and mGluR5) enhances spontaneous rhythmic bursts when synaptic inhibition is blocked in the spinal cord, and blocking mGluR I conversely lengthens the locomotor cycle period (Taccola et al., 2004). Furthermore, activation of presynaptic mGluR I causes membrane depolarization and produces rapid fluctuations of intracellular Ca^{2+} concentration, the latter of which is believed to generate rhythmic locomotion (Takahashi and Alford, 2002).

In the auditory brainstem, mGluRs are widely expressed during development and some mGluRs persist after hearing onset (review in Lu, 2014). MNTB, a critical component involved in sound localization processing in the auditory brainstem, receives its major excitatory inputs via calyxes from bushy cells in the contralateral anteroventral cochlear nucleus (AVCN) and non-calyceal inputs from unknown sources, and inhibitory inputs from multiple sources including the ipsilateral ventral nucleus of the trapezoid body (VNTB) (review in Joris and Trussell, 2018). Multiple mGluRs exert neuromodulation at MNTB synapses (review in Kopp-Scheinpflug et al., 2011). New analyses of the data from our previous studies, in which we reported mGluR I-mediated enhancement of sIPSCs (Curry et al., 2018) and sEPSCs (Peng et al., 2020), revealed that in a subpopulation of MNTB neurons, activation of mGluR I induced temporally patterned AP-dependent transmitter release. A global mGluR5 knockout mouse model was used to examine the contribution of mGluR5 to this phenomenon. To test the hypothesis that temporally patterned spike activity evoked by mGluR I activation in the presynaptic cells may underly the patterned transmitter release in MNTB, cell-attached recordings were used to examine the effects of mGluR I in VNTB neurons and AVCN bushy cells. Immunocytochemistry was used to examine the subcellular localization of mGluR1 and mGluR5 in the VNTB-MNTB pathway.

2. Methods

2.1. Ethical approval

All animal procedures were approved by the Institutional Animal Care and Use Committees at the Northeast Ohio Medical University (NEOMED) and Florida State University (FSU), and were performed in accordance with the National Institutes of Health policies on animal use. Wildtype (WT) mice, Fmr1 knockout (KO) mice (Jackson Laboratory, Stock#: 003025; B6.129P2-Fmr1^{tm1Cgr}/J), and mGluR5 KO mice (Jackson Laboratory, Stock#: 003558; B6.129-Grm5^{tm1Rod}/J) were purchased from the Jackson Laboratory and bred at NEOMED

and FSU. Genotype was confirmed with standard PCR protocol provided by the Jackson Laboratory. Genotyping was performed by Transnetyx (Cordova, TN). Mice were housed in a vivarium with a normal light-dark cycle (12 h light and 12 h dark).

2.2. Brain slice preparation and in vitro whole-cell recordings

Coronal brainstem slices (~250 μm in thickness) were prepared from 2–3 weeks old mice of both sexes, as described in our previous publications (Curry et al., 2018; Peng et al., 2020). Mice were deeply anesthetized with isoflurane and rapidly decapitated. The brainstem was removed and sliced in ice-cold low-Na^+ artificial cerebrospinal fluid (ASCF) containing the following (in mM): 250 glycerol, 3 KCl, 1.2 KH_2PO_4, 20 $NaHCO_3$, 3 HEPES, 1.2 $CaCl_2$, 5 $MgCl_2$, and 10 glucose, pH 7.4 (when gassed with 95% O_2 and 5% CO_2). Slices were incubated in an interface chamber at 34–36 °C for ~1 h in normal ACSF containing the following (in mM): 130 NaCl, 3 KCl, 1.2 KH_2PO_4, 20 $NaHCO_3$, 3 HEPES, 2.4 $CaCl_2$, 1.3 $MgSO_4$, and 10 glucose, pH 7.4. For recording, slices were transferred to a 0.5 mL chamber mounted on a Zeiss Axioskop 2 FS Plus microscope with a 40× or 63× water-immersion objective and infrared differential interference contrast optics. The chamber was continuously superfused with ACSF (2–5 mL/min) by gravity. Recordings were performed under near physiological temperatures (34–36 °C).

Patch pipettes were drawn on a PP-830 or PC-100 Microelectrode Puller (Narishige) to a 1–2 μm tip diameter using borosilicate glass micropipettes (inner diameter, 0.84 mm; outer diameter, 1.5 mm, World Precision Instruments). The electrodes had resistances between 3 and 6 MΩ when filled with internal solution. The internal solution for sIPSC/eIPSC recordings contained the following (in mM): 105 Cs-methanesulfonate, 35 CsCl, 5 EGTA, 10 HEPES, 1 $MgCl_2$, 4 ATP-Mg, 0.46 GTP-Na, with pH 7.2, adjusted with CsOH, and osmolarity around 290 mOsm/L. The internal solution for sEPSC/eEPSC recordings and current-clamp experiments contained the following (in mM): 130 K-gluconate, 4.5 $MgCl_2$, 4.4 Tris-phosphocreatine, 9 HEPES, 5 EGTA, 4 Na-ATP, 0.48 Na-GTP, with pH 7.3, adjusted with KOH, and osmolarity around 290 mOsm/L. In voltage-clamp experiments, QX-314 (5 mM) was added to the internal solution to block voltage-gated Na^+ (Na_V) channels and action currents. The liquid junction potential for the sIPSC and sEPSC recording solutions was 9.7 and 9.5 mV, respectively, and data were corrected accordingly. The experiments were performed with an AxoPatch 200B amplifier (Molecular Devices). Recordings were obtained at a holding potential of −70 and −60 mV, for sIPSCs and sEPSCs, respectively. Data were low-pass filtered at 5 kHz and digitized with a Data Acquisition Interface ITC-18 (InstruTech) at 50 kHz. Recording protocols were written and run using the acquisition and analysis software AxoGraph X (AxoGraph Scientific).

Glycinergic sIPSCs were isolated pharmacologically with bath application of antagonists for AMPARs (50 μM DNQX), NMDARs (100 μM APV), and $GABA_A$ receptors (10 μM gabazine). In contrast, sEPSCs were isolated pharmacologically with antagonists for $GABA_A$ receptors (10 μM gabazine) and glycine receptors (1 μM strychnine). For evoked synaptic current recordings, extracellular stimulation was performed using concentric bipolar electrodes with a tip core diameter of 127 μm (World Precision Instruments). For evoked IPSCs (eIPSCs), the stimulating electrode was positioned lateral and ventral to the

MNTB to activate the inhibitory afferent fibers presumably originating from the VNTB. To record evoked EPSCs (eEPSCs), the stimulating electrode was positioned at the ventral brainstem midline to activate the excitatory afferent fibers. The stimulus intensity at which the maximal synaptic response was elicited was chosen for experiments.

All chemicals were purchased from Sigma-Aldrich except for gabazine, and 3,5-DHPG, which were obtained from Tocris Bioscience (R&D Systems). 3,5-DHPG was prepared at a working concentration of 200 μM, which is at least 3-fold higher than its EC_{50} (0.7–60 μM depending on animal tissues) (review in Cartmell and Schoepp, 2000). This was expected to achieve a saturating concentration and thus full activation of mGluR I in our experiments.

2.3. Cell-attached recordings

Cell-attached recordings were made with electrodes filled with filtered (0.2 μm pore size) ACSF, under voltage-clamp mode (review in Perkins, 2006). Loose seals (sealed resistance ranging 20–1000 MΩ) were formed between the electrode and cell membrane. The recorded traces were filtered offline at 1 kHz and rectified prior to auto-correlation (Hays et al., 2011). Some cell-attached recordings were performed with electrodes filled with the internal solution used for sEPSC recordings, without QX-314. After cell-attached recordings, whole-cell mode was established to determine the intrinsic firing properties of the cells, in order to confirm cell types in AVCN using our previously published protocol (Lu et al., 2007). Bushy cells fired single APs in response to suprathreshold current injections, whereas stellate cells fired multiple APs distributed across the duration of the current injection.

2.4. Immunohistochemistry

Mice age at P14 and P21 (n=6 animals for each age) were anesthetized with a mixture of ketamine and xylazine and transcardially perfused with 0.9% saline followed by 4% paraformaldehyde in 0.1 M phosphate buffer (PB). Brains were removed from the skull, post-fixed overnight in the same fixative and then transferred to 30% sucrose in PB until they sank. Brains were sectioned in the coronal plane at a thickness of 30 μm on a freezing sliding microtome. Each section was collected in 0.01 M phosphate buffered saline (PBS). Alternate serial sections were immunocytochemically stained for anti-mGluR1 or anti-mGluR5 with synaptic markers (Table 1). Briefly, free-floating sections were incubated with primary antibody solutions diluted in PBS with 0.3% Triton X-100 overnight at 4°C, followed by Alexa-Fluor secondary antibodies (Life Technologies, Carlsbad, CA) at 1:500 for 4 hours at room temperature. Nuclear and cell body counterstains were performed together with the incubation of secondary antibodies using DAPI and NeuroTrace 640/660 (1:1000; Thermo Fisher Scientific; RRID: AB_2572212), respectively. Sections were then mounted on gelatin-coated slides and coverslipped with Fluoromount-G mounting medium® (Southern Biotech, Birmingham, AL). Images were scanned with a Leica SP8 confocal microscope (Wetzlar, Germany), using an 20x objective (NA =0.7) and 60x objective (NA =1.4). Image brightness, gamma, and contrast adjustments were performed in Adobe Photoshop (Adobe Systems, Mountain View, CA). All adjustments were applied equally to all images of the same set of staining from the same animal.

For colocalization analysis in the MNTB, images taken with 60X objective were used. Individual neurons with a clear cytoplasmic boundary, a well-defined nucleus and visible nucleolus were identified and the cell body outlined based on NeuroTrace staining. Pearson's P values were calculated for each selected cell body using the plugin Coloc2 in ImageJ2 software. Statistical comparison were performed in GraphPad Prism 6 (GraphPad, San Diego, CA).

2.5. Electrophysiology data analyses

sIPSCs and sEPSCs were detected by a template using a function for product of exponentials, $f(t)=[1 – \exp(-t/\text{rise time})] \times \exp(-t/\text{decay tau})$, where t stands for time and tau for time constant. The values of the parameters for the template to detect sIPSCs were: amplitude of −50 pA, rise time of 0.5 ms, decay tau of 1 ms, with a template baseline of 2 ms and a template length of 5 ms. The values of the parameters for the template to detect sEPSCs were: amplitude of −30 pA, rise time of 0.3 ms, decay tau of 0.5 ms, with a template baseline of 1 ms and a template length of 3 ms. These parameters were determined based on the averaged trace of visually detected synaptic events. The detection threshold was typically 2.5-fold the noise standard deviation, while minimizing false positives.

Rhythmic activity was analyzed and assessed with auto-correlation processing. The original sIPSC or sEPSC traces were filtered at 1 kHz, and rectified. A representative segment (duration of 6 s) under control and 3,5-DHPG recording conditions was auto-correlated. By definition, the autocorrelogram displays a peak value of 1.0 at time zero. The shape of the autocorrelogram informs whether the synaptic events are random in timing (a nearly flat waveform with no side peaks) or rhythmic (with apparent side peaks). The amplitude of the side peaks indicates the strength of the periodicity (the higher the peak amplitude, the stronger the rhythmic activity), and the timing of the side peaks indicates the IEIs. We measured these two parameters for the first apparent side peak, as they represent the most frequent IEI and the strongest periodicity.

Statistical analyses were performed and graphs were made with GraphPad Prism9 (GraphPad Software). Mean ± SEM (standard error of the mean) and number of cells are reported, unless otherwise indicated. Data were subject to un-paired t test, paired t test, or ANOVA. The normality of data distribution was examined with Kolmogorov-Smirnov test. The data that passed the normality test were analyzed with parametric t test, whereas data that failed the normality test were analyzed with Mann Whitney test (for un-paired t test) or Wilcoxon test (for paired t test). ANOVA was used for comparisons among three groups. The data that passed the normality test were analyzed with parametric ANOVA, whereas data that failed the normality test were analyzed with Kruskal-Wallis test. A Dunn's multiple comparisons test was used to compare the drug group (3,5-DHPG) with the control. Test $p < 0.05$ is considered statistically significant.

3. Results

The results presented in the first two figures were generated with new analyses of the data from cells recorded in our previous studies (Curry et al., 2018; Lu, 2019; Peng et al., 2020).

There are no duplications of figures or graphs that have been published in these previous publications. The rest of the data were generated in new experiments designed for this study.

3.1. Activation of mGluR I triggered temporally patterned AP-dependent glycinergic sIPSCs

Activation of mGluR I enhances spontaneous release of glycine but not GABA onto MNTB neurons via a voltage-gated sodium channel (Na_V)-dependent pathway (Curry et al., 2018), so we focused here on analysis of the glycinergic sIPSCs. While increasing the sIPSC frequency and amplitude, activation of mGluR I triggered temporally patterned AP-dependent spontaneous glycine release onto a subpopulation of MNTB neurons (18 out of 58 cells, 31%). The recordings of glycinergic sIPSCs from a representative cell in which activation of mGluR I by 3,5-DHPG (200 μM) resulted in temporally patterned AP-dependent sIPSCs are shown at different time scales (Fig. 1A). These large sIPSCs were rhythmic, with a visually detectable constant interval between two neighboring events (Fig. 1A2). The large sIPSCs were interspersed with much smaller sIPSCs, the amplitude of which approximated the reported quantal size (107 pA) (Lim et al., 2003), and the timing of which appeared random (Fig. 1A3, two large sIPSCs from the 6-s segment in A2). Distribution of the sIPSC amplitudes displayed two clusters of events, one small and the other large in amplitudes. The large events are several folds higher in amplitude (nA range) in comparison to the reported quantal size. We detected no difference in the amplitude between the maximal sIPSCs under 3,5-DHPG and the electrically evoked IPSCs (eIPSCs) recorded under the same conditions without 3,5-DHPG (Fig. 1B; maximal sIPSCs: 1.103 ± 0.176 nA, n=18; eIPSCs: 1.016 ± 0.300 nA, n=15; unpaired t test p=0.1668). This result strongly suggests that the large sIPSCs induced by 3,5-DHPG were driven by spike activity from the presynaptic cells. To quantitatively detect and analyze the rhythm or periodicity of the large sIPSCs, we performed auto-correlation of a 6-s segment recording. Autocorrelogram detected the first prominent side peak at the timing of 61 ms (Fig. 1C), which approximated the visually-detected interval between two neighboring large sIPSCs. The amplitude of the first side peak was measured to be 0.176. For a completely random release recording, no side peaks with measurable timing and peak amplitude were detected, resulting in a nearly flat autocorrelogram (data not shown). Tetrodotoxin (1 μM) elimination of the 3,5-DHPG effects (Curry et al., 2018) indicates the involvement of Na_V channels, which could also be the key player in the rhythmogenesis.

Our previous works reported similarities in terms of 3,5-DHPG modulation of sIPSCs in MNTB neurons between the knockout (KO) of Fmr1 (the gene encoding fragile X retardation protein, FMRP) and wildtype (WT) mice (Figures 1&2, and text on page 8189–8190, in Curry et al., 2018), and only subtle differences in both excitatory and inhibitory synaptic transmission at MNTB between the two genotypes (Lu, 2019). The Fmr1 KO is a mouse model for Fragile X Syndrome (review in Bear et al., 2004). The Fmr1 KO was tested here to see whether the effect of mGluR I on temporally patterned AP-dependent glycine release was accentuated, as other mGluR I-mediated effects have been reported to be exaggerated in Fmr1 KO mice (e.g., Hays et al., 2011). The percentage of cells that displayed temporally patterned sIPSCs upon 3,5-DHPG application did not differ between WT and Fmr1 KO mice (Table 2; WT: 10 out of a total of 27 recorded cells, 37%; KO:

8 out of 31 cells, 26%; Chi-square test p=0.4041), suggesting that FMRP may not play a role in the rhythmogenesis at the inhibitory synapses. We examined whether there were differences in terms of the 3,5-DHPG effect on the rhythm of sIPSCs among these cells. No significant differences were detected between WT and KO, in the first side peak interval (WT: 99 ± 16 ms, n=10; KO: 122 ± 32 ms, n=8; unpaired t test p=0.8286), or amplitude (WT: 0.127 ± 0.018, n=10; KO: 0.159 ± 0.030, n=8; unpaired t test p=0.3439). Therefore, we lumped together the WT and KO cells (n=18) in the next analysis. Among these 18 cells, 5 cells displayed detectable first side peaks in their autocorrelograms under control conditions. The average timing of the first side peaks for these five cells was 232 ± 59 ms. Under 3,5-DHPG, the average time was 109 ± 16 ms (Fig. 1D; n=18). For cells that did not display any patterned sIPSCs under control conditions, we assigned a value of zero for their peak amplitude. Paired t test detected significant difference between control and the drug group (Fig. 1E; ctr: 0.042 ± 0.084, n=18; DHPG: 0.141 ± 0.070, n=18; paired t test p=0.0016). When the IEIs were plotted sequentially in the order of event detection, the distribution of the IEIs under 3,5-DHPG showed non-exponential decay, with the peak at about 50 ms, approximately matching the timing of the first side peak (61 ms) detected in the autocorrelogram (Fig. 1F). Plotting of the IEIs against the amplitudes of sIPSCs revealed no correlation between IEI and amplitude (linear regression R^2=0.0010, p=0.1689), indicating independence of IEI on sEPSC amplitude (Fig. 1G). There was one cluster of sIPSCs that were of the smallest amplitudes and varying IEIs (green dashed oval), likely reflecting the randomness in the timing of the putative quantal release. With increasing current amplitudes, a cluster of large sIPSCs showed a relatively constant IEI around 50 ms (red dashed oval) matching approximately the timing (61.1 ms) of the first side peak detected in the autocorrelogram. This was more evident in the IEI distribution of the sIPSCs that were of amplitudes larger than 200 pA (Fig. 1G, inset).

3.2. Activation of mGluR I triggered temporally patterned bursting glutamatergic sEPSCs

Similar to the effects of 3,5-DHPG on sIPSCs, the percentage of cells that displayed temporally patterned AP-dependent sEPSCs upon 3,5-DHPG application was similar between WT and Fmr1 KO (Table 2; WT: 15 out of 95 cells, 16%; KO: 2 out of 12 cells, 17%; Chi-square p>0.9999). There was no difference in terms of the 3,5-DHPG effect on the rhythmogenesis of sEPSCs between the two genotypes, in the first side peak time (WT: 262 ± 38 ms, n=15; KO: 232 ± 33 ms, n=2; unpaired t test p=0.9632), or amplitude (WT: 0.116 ± 0.010, n=15; KO: 0.095 ± 0.009, n=2; unpaired t test p=0.8088). Therefore, we lumped together the WT and KO cells (n=17) in the analysis of the autocorrelogram data. The generation of temporally patterned sEPSCs by activation of mGluR I with 3,5-DHPG differed from that of sIPSCs in three aspects. First, temporally patterned sEPSCs were less commonly observed than temporally patterned sIPSCs (Table 2). 3,5-DHPG (200 μM) triggered temporally patterned spontaneous glutamate release onto a total of 17 out of 107 MNTB cells (16%).

Second, among the MNTB neurons that exhibited temporally patterned sEPSCs, the majority of them (11 out of 15 cells in WT, 73%, and 2 of 2 cells in KO, 100%) displayed clusters of sEPSCs, during and/or after 3,5-DHPG application. Between each pair of neighboring clusters, there was a relatively constant time gap, being about 5 s for

the sample neuron (Fig. 2A). Bursts, in which 2 or more large sEPSCs appeared closely in time, were frequently observed during 3,5-DHPG application (Fig. 2A2). For sIPSCs, few (2 out of 18 cells) displayed such bursting activity. Interspersed between the large sEPSCs were much smaller sEPSCs (Fig. 2A3), the size of which approximated the reported quantal size in mice (Inchauspe et al., 2012, 45 pA; Chang et al., 2015, 62 pA) and the timing of each event appeared random. In the histogram distribution of the sEPSC amplitudes, events of larger amplitudes were observed following the smaller events (Fig. 2A3 inset). The large sEPSCs triggered by 3,5-DHPG were of an amplitude apparently larger than the quantal size (less than 100 pA), however, they were significantly smaller than eEPSCs recorded under the same conditions without 3,5-DHPG (Fig. 2B; sEPSC: 0.494 ± 0.065 nA, n=17; eEPSC: 1.996 ± 0.371 nA, n=30, from Lu, 2019; unpaired t test, p=0.0269). These large sEPSCs appeared to match to a subpopulation of the eEPSCs of smaller amplitudes, which may be caused by non-calyceal inputs to MNTB. However, it is also worth noting that EPSCs originating from a calyx input could have an amplitude in the pA range. For example, a criteria of >300 pA at the holding potential of −60 mV has been used to define a calyceal synaptic input (Forsythe and Barnes-Davies, 1993; Barnes-Davies and Forsythe, 1995). For the sample neuron, the autocorrelogram detected the first side peak at the timing of 395 ms, which approximated the visually-detected IEI between two neighboring bursts, and the maximum amplitude of the first side peak was 0.172 (Fig. 2C).

Finally, the time, but not the amplitude, of the first side peak in the autocorrelogram differed between sEPSCs and sIPSCs. Among the 17 cells which showed temporally patterned sEPSCs under 3,5-DHPG, only 1 cell under control conditions displayed detectable first side peak in its autocorrelogram (at 163 ms), and therefore, no statistical analysis was performed on the timing of the first side peak (Fig. 2D). The average time of the first side peaks under 3,5-DHPG was 258 ± 34 ms (n=17), more than double of the average value for sIPSCs (109 ms) (unpaired t test p=0.0003; 17 and 18 cells for sEPSC and sIPSC, respectively), suggestive of less frequent temporally patterned spontaneous glutamate release compared to glycine release onto MNTB neurons in response to mGluR I modulation. For the average first side peak amplitude, we detected a significant difference between control and the drug group (Fig. 2E; ctr: 0.005 ± 0.005, n=17; DHPG: 0.113 ± 0.009, n=17; paired t test p<0.0001). Furthermore, the first side peak amplitudes of the autocorrelograms for sEPSCs under 3,5-DHPG were not different from those for sIPSCs (unpaired t test p=0.2347; 17 and 18 cells for sEPSC and sIPSC, respectively), suggesting similar modulatory strength on the temporally patterned spontaneous release of glutamate and glycine by mGluR I. The distribution of IEIs showed a prominent population of events with very small IEIs due to the clustering of large sEPSCs within the bursts. The histogram distribution of the IEIs showed two peaks in the histogram, the first of which peaked at about 20 ms matching the interval between the large sEPSCs within the bursts, and the second peak at about 200 ms (Fig. 2F), matching half of the timing of the first side peak detected in the autocorrelogram. It matched only half of the first side peak timing because there were two or more large sIPSCs in each sub-burst. Plotting of the IEIs against the amplitudes of sEPSCs revealed that the putative quantal release events (Fig. 2G, likely represented by the data points within the green dashed oval) showed a large range of IEIs, reflecting the randomness in their timing of occurrence.

The large sEPSCs within the bursts resulted in a dense population of sEPSCs with a relatively constant small IEI (Fig. 2G, the data points in the red dashed oval), reflecting the closeness in timing between sEPSCs within the bursts. The bursts of sEPSCs represented a transmitter release pattern that was different from a rhythmic release pattern without bursts. We thus further analyzed the IEI of the large sEPSCs (> 50 pA) within the bursts. Among the 17 MNTB neurons which displayed temporally patterned sEPSCs, 12 cells (71%) showed bursts of sEPSCs, as shown in the sample neuron. As expected, the IEI of the sEPSC events within the bursts (amplitude > 50 pA to exclude the majority of the miniature single-vesicle release events) was much smaller than when all the sEPSC events were included (33 ± 4 ms, n=12 vs 258 ± 34 ms, n=17).

3.3. Knockout of mGluR5 largely eliminated 3–5-DHPG effects on sIPSCs and sEPSCs

In our previous publications (Curry et al., 2018; Peng et al., 2020), we showed that the effects of 3,5-DHPG on sIPSCs and sEPSCs were blocked by mGluR1 antagonist (LY367385) and mGluR5 antagonist (MPEP). Because these mGluR1/5 antagonists (applied alone, or combined) largely eliminated the enhancement of sIPSC/sEPSC by 3,5-DHPG, no AP-dependent rhythmic sIPSC/sEPSC, which was observed when large synaptic currents were elicited by 3,5-DHPG, would remain. To further support this conclusion, we performed the same types of experiments as presented in Figure 1 and Figure 2, using a transgenic mouse line, the global mGluR5 KO mouse. The hypothesis was that in mGluR5 KO mice, the effects of 3,5-DHPG on sIPSC/sEPSC were largely diminished, eliminating the enhancement of spontaneous transmission and the rhythmogenesis in MNTB.

Using the same protocol as in our previous study (Peng et al., 2020), we examined the effects of 3,5-DHPG (200 μM) on sEPSCs of MNTB principal neurons (n=19) in mGluR5 KO mice. Bath application of 3,5-DHPG did not cause any obvious changes in sEPSCs (Fig. 3A). The averaged traces of sEPSCs under control, 3,5-DHPG, and wash conditions overlapped with each other closely (Fig. 3B), suggesting no changes in sEPSC kinetics. Interestingly, a second component of the sEPSC was seen, a likely phenotype of the mGluR5 KO, because in the WT this was rarely observed. However, the 3,5-DHPG-induced inward current remained (Fig. 3A), the amplitude of which was not different from that in the WT (Fig. 3B, WT: 31.6 ± 5.9 pA, n=15, data from Peng et al., 2020; mGluR5 KO: 27.4 ± 3.4 pA, n=16; non-paired t test p=0.8836). The unchanged inward current in the mGluR5 KO suggested that the current was primarily mediated by mGluR1, the other member of mGluR I. No significant differences were detected in sEPSC frequency (normalized to ctr) (Fig. 3D, DHPG: 1.10 ± 0.10, n=19; wash: 1.22 ± 0.14, n=17; Kruskal-Wallis test p=0.6269, Dunn's test between ctr and DHPG: p>0.9999), and normalized sEPSC amplitude (Fig. 3E, DHPG: 1.12 ± 0.12, n=19; wash: 0.97 ± 0.04, n=17; Kruskal-Wallis test p=0.3939, Dunn's test between ctr and DHPG: p>0.9999). Four out of 19 cells did show >20% increase in sEPSC frequency and amplitude without bursting events in response to 3,5-DHPG, possibly due to activation of mGluR1. In addition, we detected no differences in sEPSC rise time (Fig. 3F, ctr: 0.21 ± 0.01 ms, n=19; DHPG: 0.22 ± 0.01 ms, n=19; wash: 0.22 ± 0.01 ms, n=17; Kruskal-Wallis test p=0.5021, Dunn's test between ctr and DHPG: p>0.9999), and decay time constant (Fig. 3G, ctr: 0.23 ± 0.04 ms, n=19; DHPG: 0.25 ± 0.03 ms, n=19; wash:

0.24 ± 0.04 ms, n=17; Kruskal-Wallis test p=0.6078, Dunn's test between ctr and DHPG: p>0.9999).

Using the same protocol as in our previous study (Curry et al., 2018), we examined the effects of 3,5-DHPG (200 μM) on glycinergic sIPSCs of MNTB principal neurons (n=30) in mGluR5 KO mice. Bath application of 3,5-DHPG did not cause any obvious changes in sIPSCs (Fig. 3H, I). Under control conditions, cells exhibited sIPSCs of very low frequency with high variations (0.47 ± 0.23 Hz, n=30). Because of this small value for sIPSC frequency, the percent changes under 3,5-DHPG were largely biased by a small change in the absolute number of events, resulting in large variations in sIPSC frequency and amplitude. 3,5-DHPG caused no significant changes in the frequency and amplitude of sIPSCs in mGluR5 KO mice (Fig. 3J, DHPG: 1.90 ± 0.44, n=30; wash: 1.20 ± 0.14, n=30; Kruskal-Wallis test p=0.1065, Dunn's test between ctr and DHPG: p=0.1030), and normalized sEPSC amplitude (Fig. 3K, DHPG: 1.24 ± 0.12, n=30; wash: 1.19 ± 0.12, n=30; Kruskal-Wallis test p=0.4281, Dunn's test between ctr and DHPG: p=0.5868), without any bursting sIPSCs. We detected no changes in sIPSC kinetics, including the rise time (Fig. 3L, ctr: 0.29 ± 0.02 ms, n=30; DHPG: 0.28 ± 0.02 ms, n=30; wash: 0.27 ± 0.02 ms, n=29; Kruskal-Wallis test p=0.6739, Dunn's test between ctr and DHPG: p>0.9999), and decay time constant (Fig. 3M, ctr: 1.09 ± 0.05 ms, n=30; DHPG: 1.08 ± 0.04 ms, n=30; wash: 1.04 ± 0.05 ms, n=29; Kruskal-Wallis test p=0.4050, Dunn's test between ctr and DHPG: p>0.9999). Note that 3,5-DHPG did not result in an inward current in these sIPSC recordings, because Cs^+ used in the recording electrodes eliminated the mechanism underlying the inward current (Curry et al., 2018; dos Santos e Alhadas et al., 2020).

3.4. Cell-attached recordings in VNTB neurons revealed temporally patterned spikes in response to activation of mGluR I

The large amplitudes of the sIPSCs induced by 3,5-DHPG in MNTB neurons (Fig. 1B) imply that these synaptic events may be induced by action potentials (APs) generated at the presynaptic cells for the inhibitory inputs. If activation of mGluR I depolarized and excited the presynaptic glycinergic cells that project to MNTB and the connection between the presynaptic cell and the MNTB was intact, large sIPSCs in MNTB neurons would result. Further, it was predicted that the rhythmogenesis of presynaptic APs would match to that of the rhythmic sIPSCs in MNTB neurons. MNTB receives inhibitory inputs from multiple sources, with VNTB being one of the major sources for glycinergic inputs in the mouse (Albrecht et al., 2014). To test the idea that 3,5-DHPG triggered temporally patterned spike generation in VNTB neurons, some of which (presumably glycinergic cells) may in turn evoke patterned sIPSCs in MNTB neurons, we performed cell-attached recordings in VNTB. Unlike the conventional whole-cell recording, cell-attached recording does not disrupt the intracellular environment and preserves the signaling pathways (review in Perkins, 2006). The results revealed temporally patterned spikes in VNTB neurons in response to activation of mGluR I, in 15 out of 50 cells recorded (30%), similar to the percentage of MNTB neurons displaying large rhythmic sIPSCs upon 3,5-DHPG application (37% and 26% for WT and Fmr1 KO, respectively; Table 2). 3,5-DHPG (200 μM) triggered APs with regular IEIs and constant amplitudes (Fig. 4A). The effect was long-lasting (minutes after washout of the drug). The spikes were of a characteristic bi-phasic waveform for cell-attached

extracellular recordings (with both negative and positive components), with nearly uniform amplitudes. Autocorrelogram detected the first side peak at the timing of about 85 ms (Fig. 4B), approximating the visually-detected interval between two neighboring spikes. The amplitude of the first side peak was 0.179 for the sample cell. The average timing of the first side peak of VNTB spikes (125 ± 22 ms, n=15) was similar to that of the temporally patterned sIPSCs recorded in MNTB cells (109 ± 16 ms, n=18) (Fig. 4C, unpaired t test p=0.8518). No significant difference was detected in the amplitude of the first side peak between VNTB spikes (0.116 ± 0.018, n=15) and MNTB sIPSCs (0.141 ± 0.016, n =18) (Fig. 4D, unpaired t test p=0.2967). These results suggest a strong correlation of the rhythmic presynaptic firing in VNTB cells and the temporally patterned glycine release onto MNTB neurons (see limitations in Discussion).

3.5. Rhythmogenesis of spike activity in AVCN bushy cells in response to activation of mGluR I differed in timing from that of the large sEPSCs in MNTB neurons

MNTB neurons receive their excitatory glutamatergic inputs from calyceal terminals originating from the contralateral AVCN bushy cells (review in Joris and Trussell, 2018), as well as non-calyceal inputs from unknown sources (Banks and Smith, 1992; Smith et al., 1998; Hamann et al., 2003). The calyceal input is well known for its powerful signal transmission, with the amplitudes of AP-driven eEPSCs typically in the nA range (Borst et al., 1995; Inchauspe et al., 2012; Grande et al., 2014; Chang et al., 2015). In contrast, the non-calyceal inputs are much weaker, with eEPSCs in the pA range (Forsythe and Barnes-Davies, 1993; Hamann et al., 2003). Given that the large sEPSCs in response to 3,5-DHPG had an amplitude (average 494 pA) that was significantly smaller (~4 folds) than the eEPSCs (Fig. 2B, average 1.996 nA), the latter of which was recorded presumably from activation of a mixed population of calyceal and non-calyceal terminals, we speculated that the large sEPSCs were triggered by APs generated in excitatory neurons projecting to MNTB neurons with the non-calyceal terminals. We provided two more pieces of indirect evidence to support our speculation.

First, 3,5-DHPG-induced rhythmic spike activity in AVCN bushy cells, the axons of which form the single calyceal input to the MNTB, did not match in timing to that of the large sEPSCs in MNTB neurons upon 3,5-DHPG application. Cell-attached recordings revealed generation of spikes in AVCN bushy cells in response to activation of mGluR I, in 12 out of 38 cells (32%), with 7 cells displaying temporally patterned spike firing (18%) (Fig. 5). For the sample neuron, autocorrelogram detected the first side peak at the timing of about 25 ms, which approximated the visually-detected interval between two neighboring spikes. The amplitude of the first side peak was 0.149, showing strong periodicity of the temporally patterned spikes (Fig. 5B). However, the average timing of the first side peak of the spikes in bushy cells (72 ± 33 ms, n=7) was significantly shorter than that of the bursting sEPSCs recorded in MNTB cells (258 ± 34 ms, n=17) (Fig. 5C; unpaired t test, p=0.0035). The average amplitude of the first side peak of the spikes (0.172 ± 0.0034, n=7) was similar to the amplitude for the patterned sEPSCs recorded in MNTB cells (0.113 ± 0.009, n=17), showing no differences in population averages (Fig. 5D, unpaired t test, p=0.2033). The un-matched timing between the APs in bushy cells and the large sEPSCs

in MNTB neurons under 3,5-DHPG argued against the idea that these large sEPSCs were driven by the rhythmic APs in the bushy cells.

Second, we performed the same recordings as in Figure 2, except that this time we used "half" brainstem slices, which were obtained by cutting an intact slice into two halves along the dorsoventral midline (Fig. 6A). In such a preparation, the axons of the contralateral AVCN to the MNTB were completely severed. Surprisingly, similar to what we reported (Peng et al., 2020), bath application of 3,5-DHPG (200 μM) enhanced sEPSCs in MNTB neurons (Fig. 6B–D; normalized sEPSC frequency, 3,5-DHPG: 5.80 ± 1.14; wash 1.58 ± 0.20, Kruskal-Wallis test $p<0.0001$; Dun's comparison $p<0.0001$ between control and 3,5-DHPG, and $p=0.0060$ between 3,5-DHPG and wash, n=44. Normalized sEPSC amplitude, 3,5-DHPG: 1.84 ± 0.22; wash 1.11 ± 0.08, Kruskal-Wallis test $p=0.0114$; Dun's comparison $p=0.0398$ between control and 3,5-DHPG, and $p=0.0221$ between 3,5-DHPG and wash, n=44). Remarkably, 10 out of 44 cells (23%) displayed temporally patterned AP-dependent sEPSCs under 3,5-DHPG (Fig. 6E–H), with the average of the first side peak time being 244 ± 34 ms (n=10) and the amplitude 0.098 ± 0.010 (paired t test $p=0.0020$, n=10), as robust as the recordings in intact whole brainstem slices. These data suggest that the mGluR I-triggered temporally patterned AP-dependent sEPSCs in MNTB neurons were not dependent on the presence of the cell bodies of the AVCN bushy cells, consistent with the idea that these enhanced excitatory responses may be mediated by non-calyceal inputs from unknown sources. An alternative interpretation is that in our whole brain slice preparations, the axonal connections between AVCN and MNTB were largely severed, and therefore, no differences were expected for MNTB recordings between whole and half slices.

3.6. Age dependence of the auto-correlation strength of rhythmic activities

The animals used in our experiments were during their developmental period for hearing maturation, so we examined whether the mGluR I-triggered rhythmic neuronal activities were developmentally regulated. We plotted the 1st side peak amplitude of the rhythmic PSCs in MNTB neurons and APs in VNTB neurons against the mouse age, and performed a linear regression analysis. We detected no significant correlation between the 1st side peak amplitude of the rhythmic sIPSCs and the mouse age (Fig. 7A; $R^2=0.0471$, $p=0.3868$, n=18). Consistently, there was no significant correlation between the rhythmic APs of VNTB neurons and the mouse age (Fig. 7B; $R^2=0.1821$, $p=0.1127$), although a trend of decrease in rhythmic strength with increasing age seemed apparent. Interestingly, we detected a significant correlation between the 1st side peak of the rhythmic sEPSCs and the mouse age (Fig. 7C; $R^2=0.1675$, $p=0.0340$, n=27). However, when excluding the three data points from animals prior to hearing onset, the correlation disappeared (Fig. 7D; $R^2=0.0005$, $p=0.9166$, n=24). This suggests that there may exist a developmental shift in the rhythmic activity after hearing onset. Indeed, in 1-week old mice, rhythmogenesis of bursting sEPSCs in MNTB neurons induced by 3,5-DHPG was prominent (our unpublished data).

3.7. Expression and localization of mGluR1 and mGluR5 in the inhibitory circuit

To explore the cellular mechanisms of mGluR activation, we examined subcellular localization of the two members of mGluR I along the inhibitory VNTB-MNTB pathway in P14 and P21wildtype mice using immunocytochemistry. Specifically, we asked two

questions: 1) whether mGluR1 and mGluR5 are located in the inhibitory presynaptic terminals within MNTB, and 2) whether mGluR1 and mGluR5 are located in the cell bodies of VNTB neurons.

A previous study reported that mGluR1 immunostaining is primarily postsynaptic in the MNTB of P11–14 rats (Kushmerick et al., 2004). We observed a similar pattern in the MNTB of P14 and P21 mice. mGluR1-immunoreactive puncta were immediately apposed (but not overlapped with) synaptotagmin 2 (Syt2; Fig. 8A), a marker for presynaptic terminals Consistently, many mGluR1 puncta around MNTB cell bodies contained Homer 1 immunoreactivity (arrows in Fig. 8B), a postsynaptic density protein commonly found in glutamatergic synapses (Brakeman et al., 1997). Co-localization analyses of individual MNTB cell bodies at P14 demonstrated a significantly higher Pearson's R value for mGluR1/Homer1 (0.22 ± 0.06, n = 20 neurons) than mGluR1/Syt2 (0.06 ± 0.03, n = 12 neurons; Mann-Whitney test; $p < 0.0001$). These observations demonstrate a postsynaptic localization of mGluR1 in the MNTB at these ages. Additional mGluR1 immunoreactivity was detected within and between the cell bodies of MNTB neurons. Within the VNTB, somatic mGluR1 was identified in a small population of neurons (white asterisk in Fig. 8C). However, this localization was not evident in other VNTB neurons (yellow dot in Fig. 8C). Many mGluR1 puncta in the VNTB appeared to be postsynaptic in opposition to terminals labeled with synaptic vesicle protein 2 (SV2), a pan marker for presynaptic terminals (Fig. 8C). Together, these observations demonstrated varying degrees of mGluR1 localization in the cell bodies of VNTB, but not in their axon terminals within MNTB.

We have previously reported the presence of mGluR5 in SV2-labeled presynaptic terminals in MNTB of P14 mice (Peng et al., 2020). In this study, we further examined how presynaptic mGluR5 is associated with the terminal type in the MNTB. We detected no substantial overlapping of mGluR5 with vesicular glutamate transporter 1 (vGluT1), a marker for calyx terminals (Fig. 9A–B), indicating a non-calyceal origin. On the other hand, mGluR5 localization was detected in inhibitory terminals as evident by the presence of mGluR5 immunoreactivity in presynaptic structures containing glycine transporter 2 (GlyT2) and the vesicular GABA transporter (VGAT) (Fig. 9C). Co-localization analyses of individual MNTB cell bodies demonstrated a significantly lower Pearson's R value for mGluR5/vGluT1 (0.04 ± 0.05, n = 48 neurons) than either mGluR5/GlyT2 (0.22 ± 0.12, n = 30 neurons; Mann-Whitney test; $p < 0.0001$) or mGluR5/VGAT (0.29 ± 0.11, n = 30 neurons; Mann-Whitney test; $p < 0.0001$), supporting a preferred location of mGluR5 in inhibitory vs. excitatory presynaptic terminals in MNTB. In the VNTB, somatic mGluR5 was not immediately evident, and mGluR5 immunoreactivity was primarily located in spaces between neuronal cell bodies (Fig.9D). In the neuropil region, many mGluR5 puncta were distributed in opposition to, but not overlapping with, SV2-labeled terminals, indicating a postsynaptic localization (Fig. 9D). Together, VNTB neurons likely contained mGluR5 in their axon terminals within the MNTB but not in their cell bodies.

4. Discussion

We report here that activation of mGluR I triggered temporally patterned AP-dependent spontaneous glycine and glutamate release onto a subpopulation of MNTB neurons.

Activation of mGluR I also triggered rhythmic spike firing in VNTB neurons, the potential presynaptic cells for the inhibitory inputs to MNTB. The phenomenon is intriguing for the following reasons. First, spontaneous firing and subsequent AP-dependent transmitter release is a stochastic process, and therefore any apparent temporal pattern for spontaneous activity is unusual. Second, mGluRs typically cause long-lasting sustained but not temporally patterned responses, and therefore mGluR-triggered temporally patterned spontaneous activity is rare. Finally, the phenomenon was observed at both the excitatory and inhibitory synapses impinging upon MNTB neurons, suggesting that neural modulation mediated by mGluR I may play a role in maintaining a balance between synaptic excitation and inhibition.

4.1. Temporally patterned spontaneous synaptic activity in neural development

Prior to the appearance of APs evoked by external visual stimulation, temporally patterned spontaneous spike activity in the retina facilitates the formation of visual neural circuits during development (review in Ackman and Crair, 2014). In the mammalian auditory system, prior to hearing onset (P13 in rodents), spontaneous spike activity is originally produced in the cochlea (review in Wang and Bergles, 2015). Remarkably, the spontaneous activity bears temporal patterns. The spontaneous activity is transmitted into the central auditory system, and plays indispensable roles in circuit formation. Disruption of the spontaneous activity leads to malformation of the tonotopic map in the sound localization circuit (Müller et al., 2019). Deletion of astrocytic mGluR5 or neuronal mGluR3 (a member of mGluR II) disrupts the spontaneous spike activity in the auditory midbrain and cortex (Kellner et al., 2021), indicating the involvement of mGluRs in the generation and/or maintenance of the spontaneous activity.

Temporally patterned spontaneous activity may extend into developmental periods after sensory experience commences. In the chick, temporally patterned (bursting) spontaneous spike activity in the cochlear nucleus magnocellularis (NM) is apparent *in ovo* right around the time of hearing onset (at E15–16, equivalent to P13–14 in rodents). A few days later (at E18) the bursting pattern disappears and is replaced with a sustained tonic firing (Lippe, 1994, 1995). Cells in NM experience dramatic developmental changes in their morphology and physiology in this period (E13-E18), during which the neural properties and circuits underlying adulthood behaviors are established (review in Rubel and Fritzsch, 2002). The timing for the presence of the patterned spontaneous activity in the chick NM is comparably consistent with that for the mGluR I-induced patterned synaptic activity in the mouse auditory brainstem. Therefore, besides the peripheral mechanism accounting for the generation of patterned spontaneous activity before hearing onset, there may exist a central mechanism mediated by mGluRs that helps maintain or reinforce the temporally patterned spontaneous activity in later developmental stages.

The involvement of mGluRs and FMRP in generating or strengthening rhythmic spike activity and transmitter release has been demonstrated in studies in which these proteins are genetically manipulated. In mGluR1 KO mice, spontaneous rhythmic locomotion is reduced (Conquet et al., 1994) and blocking mGluR I activity reduces respiratory frequency in lamprey (Bongianni et al., 2002). In Fmr1 KO, cortical hyperexcitability is accompanied

by a decreased synchrony of network inhibition (Gibson et al., 2008). The reduced rhythmic activity in Fmr1 KO is rescued by the treatment with an antagonist for mGluR5 or by genetic deletion of mGluR5 (Hays et al., 2011), indicating that enhanced mGluR5 signaling underlies the reduced rhythmic activity when FMRP is dysfunctional. These studies revealed an intimate relationship between FMRP and mGluR5 in regulation of rhythmic cerebral activity. However, FMRP did not seem to contribute to the rhythmogenesis of sIPSCs or sEPSCs in MNTB.

4.2. Potential mechanisms underlying mGluR-triggered patterned firing and transmitter release

mGluR-induced patterned spike firing and transmitter release may involve signaling pathways leading to modulation of multiple ion channels, with a dominant involvement of a persistent voltage-gated Na^+ channel current (I_{NaP}) and ion channel-mediated Ca^{2+} signaling. The I_{NaP} plays a significant role in the generation of the respiratory rhythm *in vitro* (Koizumi and Smith, 2008), as well as in pacemaking in globus pallidus neurons (Mercer et al., 2007). In external tufted cells in the olfactory bulb, activation of mGluR I increases the firing frequency within the rhythmic bursting of APs via enhancement of Ca^{2+}-dependent non-selective cation currents (Dong et al., 2009) and I_{NaP} (Dong and Ennis, 2014). In subthalamic nucleus neurons, mGluR-induced burst firing is mediated by I_{NaP} activated at subthreshold voltages (Bevan and Wilson, 1999), or by Ca_V channels and Ca^{2+}-activated inward currents (Beurrier et al., 1999). Of important relevance, I_{NaP} exists in calyxes and the current boosts glutamate release onto MNTB neurons (Huang and Trussell, 2008). Similar expression of such a conductance on non-calyceal glutamatergic terminals might exist, although no evidence has been reported. Burst firing in cortical interneurons is evoked via mGluR1-induced Ca^{2+} signaling pathway in neocortical pyramidal cells (Czarnecki et al., 2007). In the neocortex, mGluR I and muscarinic receptors trigger synchronized firing in electrically coupled interneurons, resulting in rhythmic sIPSPs in their target cells (Beierlein et al., 2000; Deans et al., 2001). Such mGluR- and muscarinic ACh receptor-mediated patterned burst firing has been also reported in thalamocortical neurons (Hughes et al., 2008).

The mechanisms of mGluR-triggered temporally patterned AP-dependent spontaneous glycine release onto MNTB are not completely clear. Our data obtained with cell-attached recordings provided indirect evidence for the presynaptic somatic loci of mGluR I-triggered patterned spike activities in the VNTB (Fig. 4). The mGluR-triggered temporally patterned sIPSCs in MNTB are likely the result of mGluR-triggered temporally patterned spikes in VNTB glycinergic neurons (but see limitations below). The percentage of MNTB cells that showed mGluR-triggered temporally patterned AP-dependent sIPSCs was about the same as the percentage of VNTB cells that fired mGluR-induced temporally patterned APs. More importantly, the IEIs of the spike activity matched approximately the IEIs of the large sIPSCs observed in the postsynaptic MNTB neurons (Fig. 4). However, one single MNTB neuron could receive convergent inputs from more than one VNTB neurons. In that case, if the VNTB neurons with convergent inputs onto the same MNTB neuron shared similar IEIs in their mGluR-induced spikes, the correlation between the rhythmic VNTB spikes and MNTB sIPSCs would be maintained. In contrast, if the VNTB neurons projecting to

the same MNTB neuron had different IEIs in their mGluR-induced spikes, the correlation would be lost, but a more complicated temporal pattern might be generated. It awaits further investigation to determine which scenario is the case and which is more physiologically relevant. Our anatomical data supported the physiological results in that group I mGluRs were present in the cell bodies and axonal terminals of the VNTB projection upon the MNTB. The distinct preference of mGluR1 in the cell bodies of MNTB neurons and mGluR5 in the axon terminals innervating MNTB suggests that the two members of mGluR I may exert differential actions to facilitate site-specific modulation effects. The elimination of 3,5-DHPG effects on both sIPSCs and sEPSCs of MNTB in the mGluR5 KO mice (Fig. 3) indicates a dominant role of mGluR5 in the regulation of synaptic transmission, whereas the retention of the 3,5-DHPG-induced inward current in MNTB of the mGluR5 KO (Fig. 3C) supports a dominant role of mGluR1 in the regulation of intrinsic properties.

The mechanisms of mGluR-triggered temporally patterned AP-dependent spontaneous glutamate release onto MNTB are elusive. For the following three reasons, we suspect that the non-calyceal glutamatergic inputs to the MNTB may be responsible for the rhythmic large sEPSCs under mGluR I activation. First, besides receiving the calyceal glutamatergic inputs, MNTB neurons also receive non-calyceal glutamatergic inputs (Banks and Smith, 1992; Smith et al., 1998; Hamann et al., 2003). The eEPSCs mediated by the non-calyceal inputs are of much smaller amplitude than those mediated by the calyceal inputs, with the former usually in the pA range (Forsythe and Barnes-Davies, 1993; Hamann et al., 2003), and the latter in the nA range (Borst et al., 1995; Inchauspe et al., 2012; Chang et al., 2015; Grande et al., 2014). The large sEPSCs we recorded under 3,5-DHPG application appeared to be similar in amplitude to the eEPSCs mediated by the non-calyceal inputs. Second, cell-attached recordings provided indirect evidence against the presynaptic somatic loci of mGluR I-triggered patterned spike activity in the AVCN (Fig. 5), because the IEIs of the spike activity in AVCN bushy cells were significantly shorter than the IEIs of the large sEPSCs in MNTB neurons. Finally, the mGluR I-induced enhancement and rhythmogenesis of sEPSCs in MNTB neurons did not depend on the presence of cell bodies in the AVCN (Fig. 6), pointing to a possible dependence on non-calyceal inputs. The sources of the non-calyceal inputs to MNTB are not known, although it was suggested that cells located within the superior olivary complex (Banks and Smith, 1992), or axonal collaterals of bushy cells may give rise to these inputs (Forsythe and Barnes-Davies, 1993). Although we propose that the non-calyceal inputs mediated the large sEPSCs under 3,5-DHPG, we cannot exclude the possibility that compound vesicle fusion may occur inside the calyceal terminals, resulting in increased quantal size (a few hundreds of pA in amplitude) (He et al., 2009).

4.3. Functional implications

We speculate that temporally patterned synaptic activities in the sound localization circuit may facilitate the establishment of the neural properties essential for temporal coding (e.g., phase-locking), in addition to forming the tonotopic organization of auditory neural circuits (Clause et al., 2014; Bach and Kandler, 2020). In hippocampal CA1 pyramidal neurons, mGluR5 activation improves spike timing and temporal precision in local neural circuits via enhancement of I_{NaP} (Yu et al., 2018a, b). Temporally patterned synaptic inhibition can coordinate the timing of APs, resulting in timely precise phasic inhibition which

functions to sculpt the spike timing for the excitatory inputs (Cobb et al., 1995). In MNTB, precisely timed excitation as well as timed inhibition are important neuronal features for auditory temporal processing (review in Grothe et al., 2010). Besides its potential roles in development of neural circuits, the mGluR-triggered patterned AP-dependent spontaneous transmitter release was observed at both excitatory and inhibitory synapses in MNTB, suggesting that such modulation plays a role in maintenance of the balance between excitation and inhibition. The IEIs of the temporally patterned events, however, differ substantially in their absolute values between the sEPSCs and sIPSCs, pointing to differential modulation as well as independent functions for the modulation of mGluRs on the excitatory vs inhibitory transmission. Interestingly, only a subpopulation of MNTB neurons displayed mGluR I-triggered temporally patterned spontaneous synaptic responses while others showed increased responses without any apparent temporal patterns. Similarly, mGluR-triggered spike firing in cortical interneurons and subsequent sIPSPs in their target neurons could be either irregular or patterned in their temporal structure (Beierlein et al., 2000). Differential expression of mGluR I and/or I_{NaP} in the presynaptic neurons may underlie the different propensity of the generation of temporally patterned spike activities. Further, the existence of temporally patterned transmitter release onto a subpopulation of MNTB neurons may be sufficient in facilitating functional establishment of neural circuits, by recruiting neural network via gap junction channels in early development. Finally, mGluR I-triggered temporally patterned spontaneous transmitter release was very prominent in early development (P7–10) in MNTB neurons (our unpublished observation), warranting further investigation of their roles in the establishment of neural circuits prior to hearing onset.

4.4. Limitations of the current study

We recognize limitations of our study. First, we did not identify the cell types recorded in VNTB. In non-mouse rodent species, VNTB consists of a mixed cell population in terms of transmitter phenotypes including glycinergic, GABAergic, and cholinergic cells (Helfert et al., 1989; Yao and Godfrey, 1998; Gómez-Nieto et al., 2008). In the mouse, the existence of glycinergic cells in VNTB and their inhibitory projections to the ipsilateral MNTB have been confirmed (Albrecht et al., 2014). The reported intrinsic neural properties of mouse VNTB neurons have not yet offered criteria to distinguish cell types in the nucleus (Sinclair et al., 2017). Therefore, our cell-attached recordings from the VNTB inevitably contained mixed cell types. The second limitation is that the sources of the excitatory inputs mediating the large sEPSCs enhanced by 3,5-DHPG were not identified. Third, the MNTB neurons we recorded were primarily collected from the low and middle frequency-coding parts of the nucleus, preventing us from determining whether there exists a tonotopic organization in the mGluR modulation. Fourth, the application of 3,5-DHPG was of a prolonged time, which may not closely mimic the physiological condition in vivo under which glutamate is released in a much briefer period. However, given that the spontaneous spike activity at the mouse calyx-MNTB synapse in vivo is high (70 Hz, Lorteije et al., 2009), sustained activation of mGluR I and subsequent generation of temporally patterned AP-dependent transmitter release might be highly possible. Such patterned activity may play a similar role as the cochlea-originated spontaneous activity in the auditory system prior to hearing onset (review in Wang and Bergles, 2015). Fifth, for historical reasons, we used a higher-than

physiological calcium concentration (2.4 mM) in ACSF. In mouse CSF, the physiological calcium concentration is about 1.2 mM (Ding et al., 2016). High calcium is known to presynaptically promote multiquantal release (Budisantoso et al., 2013) and postsynaptically reduce cellular excitability (review in Jones and Smith, 2016). Therefore, our physiological data were collected under a high release probability and low cellular excitability condition, although we do have limited data showing similar phenomenon regarding 3,5-DHPG modulation of sEPSCs when using 1.2 mM calcium (data not shown). Finally, the loci of mGluR1/5 in MNTB and VNTB were determined with light microscopy not electronic microscopy. Typically these mGluRs are expressed postsynaptically, but here we reported presynaptic mGluR5, which is consistent with its effects on increasing the frequency of transmitter release, an indicator for presynaptic actions. Although not common, presynaptic mGluR5 expression and its modulation of calcium signaling and synaptic transmission have been demonstrated in multiple neural circuits (Kim et al., 2009; Xie et al., 2017; Colmers and Bains, 2018; Fernandes et al., 2021).

Acknowledgments

We thank Lin Cai for editorial assistance. This work was supported by National Institute of Health Grant R01DC016054 (YL), NEOMED Bridge Fund (YL), and R01MH126176 (YW).

Data Availability Statement

The datasets generated for this study are available on request to the corresponding author.

Abbreviations

ACSF	artificial cerebrospinal fluid
AP	action potential
AVCN	anteroventral cochlear nucleus
eEPSC/eIPSC	evoked excitatory/inhibitory postsynaptic current
FMRP	fragile X retardation protein
GPCR	G-protein-coupled receptor
IEI	inter-event interval
mGluR I	group I metabotropic glutamate receptor
I_{NaP}	persistent voltage-gated Na^+ channel current
KO	knockout
MNTB	medial nucleus of the trapezoid body
Na_V channel	voltage-gated Na^+ channel
NM	nucleus of magnocellularis

sEPSC/sIPSC	spontaneous excitatory/inhibitory postsynaptic current
VNTB	ventral nucleus of the trapezoid body
WT	wildtype

References

Ackman JB, Crair MC, 2014. Role of emergent neural activity in visual map development. Curr. Opin. Neurobiol 24, 166–175. [PubMed: 24492092]

Albrecht O, Dondzillo A, Mayer F, Thompson JA, Klug A, 2014. Inhibitory projections from the ventral nucleus of the trapezoid body to the medial nucleus of the trapezoid body in the mouse. Front. Neural Circuits 8, 83. [PubMed: 25120436]

Bach EC, Kandler K, 2020. Long-term potentiation of glycinergic synapses by semi-natural stimulation patterns during tonotopic map refinement. Sci. Rep 10:16899. [PubMed: 33037263]

Banks MI, Smith PH, 1992. Intracellular recordings from neurobiotin-labeled cells in brain slices of the rat medial nucleus of the trapezoid body. J. Neurosci 12, 2819–2837. [PubMed: 1351938]

Barnes-Davies M, Forsythe ID, 1995. Pre- and postsynaptic glutamate receptors at a giant excitatory synapse in rat auditory brainstem slices. J. Physiol 488, 387–406. [PubMed: 8568678]

Bear MF, Huber KM, Warren ST, 2004. The mGluR theory of fragile X mental retardation. Trends Neurosci 27, 370–377. [PubMed: 15219735]

Beierlein M, Gibson JR, Connors BW, 2000. A network of electrically coupled interneurons drives synchronized inhibition in neocortex. Nat. Neurosci 3, 904–910. [PubMed: 10966621]

Beurrier C, Congar P, Bioulac B, Hammond C, 1999. Subthalamic nucleus neurons switch from single-spike activity to burst-firing mode. J. Neurosci 19, 599–609. [PubMed: 9880580]

Bevan MD, Wilson CJ, 1999. Mechanisms underlying spontaneous oscillation and rhythmic firing in rat subthalamic neurons. J. Neurosci, 19, 7617–7628. [PubMed: 10460267]

Bongianni F, Mutolo D, Carfi M, Pantaleo T, 2002. Group I and II metabotropic glutamate receptors modulate respiratory activity in the lamprey. Eur. J. Neurosci 16, 454–460. [PubMed: 12193188]

Borst JG, Helmchen F, Sakmann B, 1995. Pre- and postsynaptic whole-cell recordings in the medial nucleus of the trapezoid body of the rat. J. Physiol 489, 825–840. [PubMed: 8788946]

Brakeman PR, Lanahan AA, O'Brien R, Roche K, Barnes CA, Huganir RL, Worley PF, 1997. Homer: a protein that selectively binds metabotropic glutamate receptors. Nature 386, 284–288. [PubMed: 9069287]

Budisantoso T, Harada H, Kamasawa N, Fukazawa Y, Shigemoto R, Matsui K 2013. Evaluation of glutamate concentration transient in the synaptic cleft of the rat calyx of Held. J. Physiol 591, 219–239. [PubMed: 23070699]

Cartmell J, Schoepp DD, 2000. Regulation of neurotransmitter release by metabotropic glutamate receptors. J. Neurochem 75, 889–907. [PubMed: 10936169]

Chang S, Reim K, Pederson M, Neher E, Brose N, Taschenberger H, 2015. Complexin stabilizes newly primed synaptic vesicles and prevents their premature fusion at the mouse calyx of Held synapse. J. Neurosci 35, 8272–8290. [PubMed: 26019341]

Clause A, Kim G, Sonntag M, Weisz CJC, Vetter DE, Rübsamen R, Kandler K, 2014. The precise temporal pattern of prehearing spontaneous activity is necessary for tonotopic map refinement. Neuron 82, 822–835. [PubMed: 24853941]

Cobb SR, Buhl EH, Halasy K, Paulsen O, Somogyi P, 1995. Synchronization of neuronal activity in hippocampus by individual GABAergic interneurons. Nature 378, 75–78. [PubMed: 7477292]

Cohen I, Kita H, Van Der Kloot W, 1974. The stochastic properties of spontaneous quantal release of transmitter at the frog neuromuscular junction. J. Physiol 236, 341–361. [PubMed: 16992438]

Colmers PL, Bains JS, 2018. Presynaptic mGluRs control the duration of endocannabinoid-mediated DSI. J. Neurosci 38, 10444–10453. [PubMed: 30355625]

Curry RJ, Peng K, Lu Y, 2018. Neurotransmitter- and release-mode-specific modulation of inhibitory transmission by group I metabotropic glutamate receptors in central auditory neurons of the mouse. J. Neurosci 38, 8187–8199. [PubMed: 30093538]

Conquet F, Bashir ZI, Davies CH, Daniel H, Ferraguti F, Bordi F, Franz-Bacon K, Reggiani A, Matarese V, Condé F, Collingridge L, Crépel F, 1994. Motor deficit and impairment of synaptic plasticity in mice lacking mGluR1. Nature 372, 237–243. [PubMed: 7969468]

Czarnecki A, Birtoli B, Ulrich D, 2007. Cellular mechanisms of burst firing-mediated long-term depression in rat neocortical pyramidal cells. J. Physiol 578, 471–479. [PubMed: 17082228]

Deans MR, Gibson JR, Sellitto C, Connors BW, Paul DL, 2001. Synchronous activity of inhibitory networks in neocortex requires electrical synapses containing connexin36. Neuron 31, 477–485. [PubMed: 11516403]

Del Negro CA, Funk GD, Feldman JL, 2018. Breathing matters. Nat. Rev. Neurosci 19, 351–367. [PubMed: 29740175]

Ding F, O'Donnell J, Xu Q, Kang N, Goldman N, Nedergaard M 2016. Changes in the composition of brain interstitial ions control the sleep-wake cycle. Science 352, 550–555. [PubMed: 27126038]

Dong HW, Ennis M, 2014. Activation of group I metabotropic glutamate receptors enhances persistent sodium current and rhythmic bursting in main olfactory bulb external tufted cells. J. Neurophysiol 111, 641–647. [PubMed: 24225539]

Dong HW, Hayar A, Callaway J, Yang XH, Nai Q, Ennis M, 2009. Group I mGluR activation enhances Ca^{2+}-dependent nonselective cation currents and rhythmic bursting in main olfactory bulb external tufted cells. J. Neurosci 29, 11943–11953. [PubMed: 19776280]

dos Santos e Alhadas É, Correa AMB, Naves LA, Kushmerick C, 2020. Mechanisms and functional impact of group I metabotropic glutamate receptor modulation of excitability in mouse MNTB neurons. Synapse 2020;74:e22137. [PubMed: 31584700]

El Manira A, Kettunen P, Hess D, Krieger P, 2002. Metabotropic glutamate receptors provide intrinsic modulation of the lamprey locomotor network. Brain Res. Rev 40, 9–18. [PubMed: 12589902]

Fernandes G, Mishra PK, Nawaz MS, Donlin-Asp PG, Rahman MM, Hazra A, Kedia S, Kayenaat A, Songara D, Wyllie DA, Schuman EM, Kind PC, Chattarji S, 2021. Correction of amygdalar dysfunction in a rat model of fragile X syndrome. Cell Rep 37, 109805. [PubMed: 34644573]

Forsythe ID, Barnes-Davies M, 1993. The binaural auditory pathway: excitatory amino acid receptors mediate dual timecourse excitatory postsynaptic currents in the rat medial nucleus of the trapezoid body. Proc. Biol. Sci 251, 151–157. [PubMed: 8096081]

Gibson JR, Bartley AF, Hays SA, Huber KM, 2008. Imbalance of neocortical excitation and inhibition and altered UP states reflect network hyperexcitability in the mouse model of fragile X syndrome. J. Neurophysiol 100, 2615–2626. [PubMed: 18784272]

Gómez-Nieto R, Rubio ME, López DE, 2008. Cholinergic input from the ventral nucleus of the trapezoid body to cochlear root neurons in rats. J. Comp. Neurol 506, 452–468. [PubMed: 18041785]

Grande G, Negandhi J, Harrison RV, Wang LY, 2014. Remodelling at the calyx of Held-MNTB synapse in mice developing with unilateral conductive hearing loss. J. Physiol 592, 1581–1600. [PubMed: 24469075]

Grothe B, Pecka M, McAlpine D, 2010. Mechanisms of sound localization in mammals. Physiol. Rev 90, 983–1012. [PubMed: 20664077]

Grund M, Al E, Pabst M, Dabbagh A, Stephani T, Nierhaus T, Gaebler M, Villringer A, 2022. Respiration, heartbeat, and conscious tactile perception. J. Neurosci 42, 643–656. [PubMed: 34853084]

Hamann M, Billups B, Forsythe ID, 2003. Non-calyceal excitatory inputs mediate low fidelity synaptic transmission in rat auditory brainstem slices. Eur. J. Neurosci 18, 2899–2902. [PubMed: 14656340]

Hays SA, Huber KM, Gibson JR, 2011. Altered neocortical rhythmic activity states in Fmr1 KO mice are due to enhanced mGluR5 signaling and involve changes in excitatory circuitry. J. Neurosci 31, 14223–14234. [PubMed: 21976507]

He L, Xue L, Xu J, McNeil BD, Bai L, Melicoff E, Adachi R, Wu LG, 2009. Compound vesicle fusion increases quantal size and potentiates synaptic transmission. Nature 459, 93–97. [PubMed: 19279571]

Heil P, Peterson AJ, 2017. Spike timing in auditory-nerve fibers during spontaneous activity and phase locking. Synapse 71, 5–36. [PubMed: 27466786]

Helfert RH, Bonneau JM, Wenthold RJ, Altschuler RA, 1989. GABA and glycine immunoreactivity in the guinea pig superior olivary complex. Brain Res 501, 269–286. [PubMed: 2819441]

Hughes SW, Errington A, Lõrincz ML, Kékesi KA, Juhász G, Orbán G, Cope DW, Crunelli V, 2008. Novel modes of rhythmic burst firing at cognitively-relevant frequencies in thalamocortical neurons. Brain Res 1235, 12–20. [PubMed: 18602904]

Huang H, Trussell LO, 2008. Control of presynaptic function by a persistent Na^+ current. Neuron 60, 975–979. [PubMed: 19109905]

Inchauspe CG, Urbano FJ, Di Guilmi MN, Ferrari MD, van den Maagdenberg AM, Forsythe ID, Uchitel OD, 2012. Presynaptic $Ca_V2.1$ calcium channels carring familial hemiplegic migraine mutation R192Q allow faster recovery from synaptic depression in mouse calyx of Held. J. Neurophysiol 108, 2967–2976. [PubMed: 22956801]

Jones BJ, Smith SM 2016. Calcium-sensing receptor: a key target for extracellular calcium signaling in neurons. Front. Physiol 7:116. [PubMed: 27065884]

Joris PX, Trussell LO, 2018. The calyx of Held: a hypothesis on the need for reliable timing in an intensity-difference encoder. Neuron 100, 534–549. [PubMed: 30408442]

Kavalali ET, 2015. The mechanisms and functions of spontaneous neurotransmitter release. Nat. Rev. Neurosci 16, 5–16. [PubMed: 25524119]

Kellner V, Kersbergen CJ, Li S, Babola TA, Saher G, Bergles DE, 2021. Dual metabotropic glutamate receptor signaling enables coordination of astrocyte and neuron activity in developing sensory domains. Neuron 109, 2545–2555. [PubMed: 34245686]

Kim YH, Park CK, Back SK, Lee CJ, Hwang SJ, Bae YC, Na HS, Kim JS, Jung SJ, Oh SB, 2009. Membrane-delimited coupling of TRPV1 and mGluR5 on presynaptic terminals of nociceptive neurons. J. Neurosci 29, 10000–10009. [PubMed: 19675234]

Koizumi H, Smith JC, 2008. Persistent Na^+ and K^+-dominated leak currents contribute to respiratory rhythm generation in the pre-Bötzinger complex in vitro. J. Neurosci 28, 1773–1785. [PubMed: 18272697]

Kopp-Scheinpflug C, Steinert JR, Forsythe ID, 2011. Modulation and control of synaptic transmission across the MNTB. Hear. Res 279, 22–31. [PubMed: 21397677]

Kushmerick C, Price GD, Taschenberger H, Puente N, Renden R, Wadiche JI, Duvoisin RM, Grandes P, von Gersdorff H, 2004. Retroinhibition of presynaptic Ca^{2+} currents by endocannabinoids released via postsynaptic mGluR activation at a calyx synapse. J. Neurosci 24, 5955–5965. [PubMed: 15229243]

Leão RM, 2019. The ion channels and synapses responsible for the physiological diversity of mammalian lower brainstem auditory neurons. Hear Res 376, 33–46. [PubMed: 30606624]

Lim R, Oleskevich S, Few AP, Leao RN, Walmsley B, 2003. Glycinergic mIPSCs in mouse and rat brainstem auditory nuclei: modulation by ruthenium red and the role of calcium stores. J. Physiol 546, 691–699. [PubMed: 12562997]

Lippe WR, 1994. Rhythmic spontaneous activity in the developing avian auditory system. J. Neurosci 14, 1486–1495. [PubMed: 8126550]

Lippe WR, 1995. Relationship between frequency of spontaneous bursting and tonotopic position in the developing avian auditory system. Brain Res 703, 205–213. [PubMed: 8719634]

Lorteije JA, Ruru SI, Kushmerick C, Borst JG, 2009. Reliability and precision of the mouse calyx of Held synapse. J. Neurosci 29, 13770–13784. [PubMed: 19889989]

Lu Y, 2014. Metabotropic glutamate receptors in auditory processing. Neuroscience 274, 429–445. [PubMed: 24909898]

Lu Y, 2019. Subtle differences in synapitc transmission in medial nucleus of trapezoid body neurons between wild-type and Fmr1 knockout mice. Brain Res 1717, 95–103. [PubMed: 31004576]

Lu Y, Harris JA, Rubel EW, 2007. Development of spontaneous miniature EPSCs in mouse AVCN neurons during a critical period of afferent-dependent neuron survival. J. Neurophysiol 97, 635–646. [PubMed: 17079338]

Mercer JN, Chan CS, Tkatch T, Held J, Surmeier DJ, 2007. Nav1.6 sodium channels are critical to pacemaking and fast spiking in globus pallidus neurons. J. Neurosci 27, 13552–13566. [PubMed: 18057213]

Moore JD, Kleinfeld D, Wang F, 2014. How the brainstem controls orofacial behaviors comprised of rhythmic actions. Trends Neurosci 37, 370–380. [PubMed: 24890196]

Müller NIC, Sonntag M, Maraslioglu A, Hirtz JJ, Friauf E, 2019. Topographic map refinement and synaptic strengthening of a sound localization circuit require spontaneous peripheral activity. J. Physiol 597, 5469–5493. [PubMed: 31529505]

Nistri A, Ostroumov K, Sharifullina E, Taccola G, 2006. Tuning and playing a motor rhythm: how metabotropic glutamate receptors orchestrate generation of motor patterns in the mammalian central nervous system. J. Physiol 572, 323–334. [PubMed: 16469790]

Niswender CM, Conn PJ, 2010. Metabotropic glutamate receptors: physiology, pharmacology, and disease. Annu. Rev. Pharmacol. Toxicol 50, 295–322. [PubMed: 20055706]

Peng K, Wang X, Wang Y, Li D, Huang H, Lu Y, 2020. Mechanisms underlying enhancement of spontaneous glutamate release by group I mGluRs at a central auditory synapse. J. Neurosci 40, 7027–7042. [PubMed: 32801152]

Perkins KL, 2006. Cell-attached voltage-clamp and current-clamp recording and stimulation techniques in brain slices. J. Neurosci. Methods 154, 1–18. [PubMed: 16554092]

Rubel EW, Fritzsch B, 2002. Auditory system development: primary auditory neurons and their targets. Annu. Rev. Neurosci 25, 51–101. [PubMed: 12052904]

Shamir M, 2019. Theories of rhythmogenesis. Curr. Opin. Neurobiol 58, 70–77. [PubMed: 31408837]

Sinclair JL, Barnes-Davies M, Kopp-Scheinpflug C, Forsythe ID, 2017. Strain-specific differences in the development of neuronal excitability in the mouse ventral nucleus of the trapezoid body. Hear. Res 354, 28–37. [PubMed: 28843833]

Smith PH, Joris PX, Yin TC, 1998. Anatomy and physiology of principal cells of the medial nucleus of the trapezoid body (MNTB) of the cat. J. Neurophysiol 79, 3127–3142. [PubMed: 9636113]

Taccola G, Marchetti C, Nistri A, 2004. Modulation of rhythmic patterns and cumulative depolarization by group I metabotropic glutamate receptors in the neonatal rat spinal cord in vitro. Eur. J. Neurosci 19, 533–541. [PubMed: 14984404]

Takahashi M, Alford S, 2002. The requirement of presynaptic metabotropic glutamate receptors for the maintenance of locomotion. J. Neurosci 22, 3692–3699. [PubMed: 11978845]

Wang HC, Bergles DE, 2015. Spontaneous activity in the developing auditory system. Cell Tissue Res 361, 65–75. [PubMed: 25296716]

Wei XP, Collie M, Dempsey B, Fortin G, Yackle K, 2022. A novel reticular node in the brainstem synchronizes neonatal mouse crying with breathing. Neuron 110, 644–657. [PubMed: 34998469]

Xie JD, Chen SR, Pan HL, 2017. Presynaptic mGluR5 receptor controls glutamatergic input through protein kinase C-NMDA receptors in paclitaxel-induced neuropathic pain. J. Biol. Chem 292, 20644–20654. [PubMed: 29074619]

Yao W, Godfrey DA, 1998. Immunohistochemical evaluation of cholinergic neurons in the rat superior olivary complex. Microsc. Res. Tech 41, 270–283. [PubMed: 9605344]

Yu W, Kwon J, Sohn JW, Lee SH, Kim S, Ho WK, 2018a. mGluR5-dependent modulation of dendritic excitability in CA1 pyramidal neurons mediated by enhancement of persistent Na^+ currents. J. Physiol 596, 4141–4156. [PubMed: 29870060]

Yu W, Sohn JW, Kwon J, Lee SH, Kim S, Ho WK, 2018b. Enhancement of dendritic persistent Na^+ currents by mGluR5 leads to an advancement of spike timing with an increase in temporal precision. Mol. Brain 11:67. [PubMed: 30413218]

Highlights

- mGluR I activation triggered temporally patterned sIPSC/sEPSC in MNTB neurons.
- Knockout of mGluR5 eliminated the effects.
- mGluR I activation generated temporally patterned action potentials in VNTB neurons.
- The effects of mGluR I on sEPSCs did not depend on the contralateral AVCN.
- Inhibitory presynaptic but not calyceal terminals contained mGluR5.

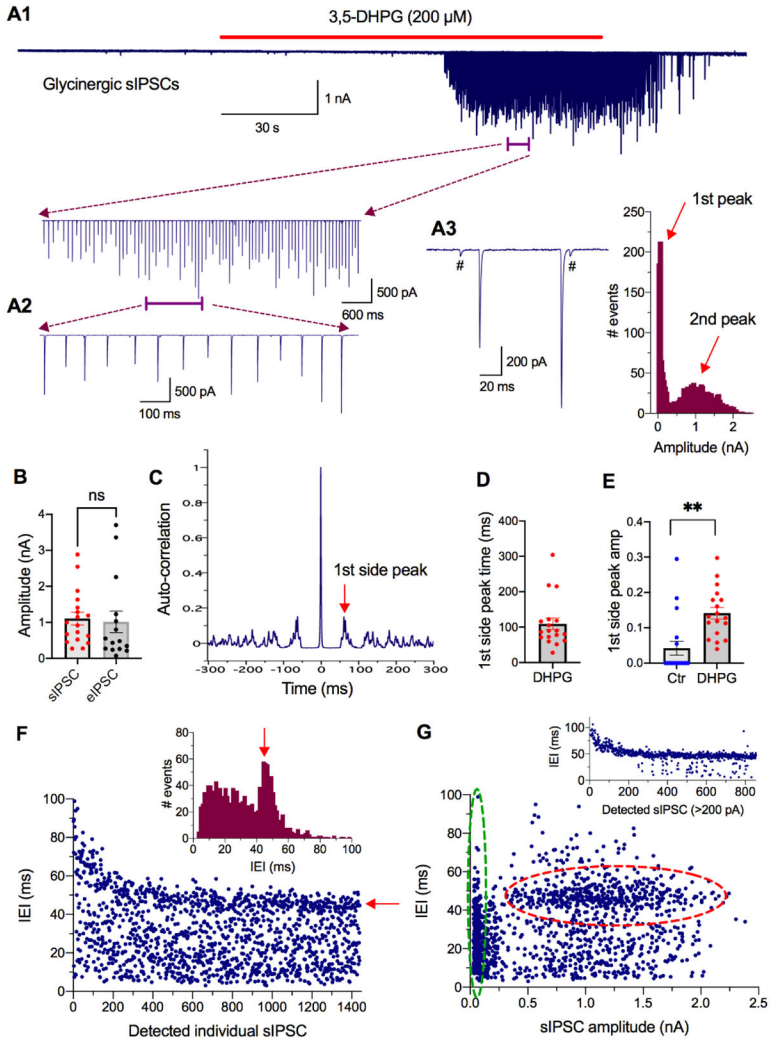

Figure 1.

Activation of mGluR I triggered temporally patterned AP-dependent spontaneous glycine release onto a subpopulation of MNTB neurons (18 out of 58 cells, 31%). (**A**) Activation of mGluR I by 3,5-DHPG (200 μM) resulted in temporally patterned sIPSCs of large amplitudes (A1). The large sIPSCs were rhythmic, with a visually detectable constant interval between two neighboring events (A2). The large sIPSCs were interspersed with much smaller sIPSCs, the size of which approximates the quantal size and the timing of which appeared random (A3, indicated by the symbol #). The histogram of the sIPSC amplitudes displays one cluster of events with small values, and a second cluster of events of larger events. (**B**) The average amplitude of the maximal sIPSCs under 3,5-DHPG (n=18) was not different from that of the eIPSCs under control conditions (n=15; unpaired t test p=0.1688), suggesting that the large sIPSCs under 3,5-DHPG were AP driven. (**C**) Autocorrelogram detected the first side peak at the timing of 61 ms, which approximates the visually-detected interval between two neighboring large sIPSCs in A2. The amplitude of the first side peak, representing the strength of the periodicity for rhythmic release, was 0.176. (**D**) The timing of the first side peaks, representing the interval of the rhythmic

sIPSCs, was 109 ms (n=18) under 3,5-DHPG. (**E**) Paired t test detected significant difference in the first side peak amplitude between control and drug group (p=0.0016; n=18). Note that under control conditions, most cells did not have side peaks in their autocorrelograms, and the amplitude was assigned a value of zero. (**F**) When the IEIs were plotted sequentially in the order of event detection, the distribution of the IEIs of the sample cell showed a peak at about 50 ms (indicated by the red arrows in the main graph and the inset), approximately matching the interval between two large neighboring sIPSCs. (**G**) Plotting of the IEIs against the amplitudes of sIPSCs of the sample cell. There was one group of sIPSCs that were of the smallest amplitudes (likely quantal size, <100 pA) and a large range of varying IEIs (green dashed oval), reflecting the randomness in timing of the quantal release. With increasing amplitudes, a group of large sIPSCs showed a constant IEI of about 50 ms (red dashed oval; also see the inset), matching the timing of the first side peak in the autocorrelogram. Mean ± SEM are shown in this and subsequent figures. ns: not significant; * $p < 0.05$, ** $p < 0.01$, *** $p < 0.001$ (paired or unpaired t test). Cells were held at −70 mV for IPSC recordings.

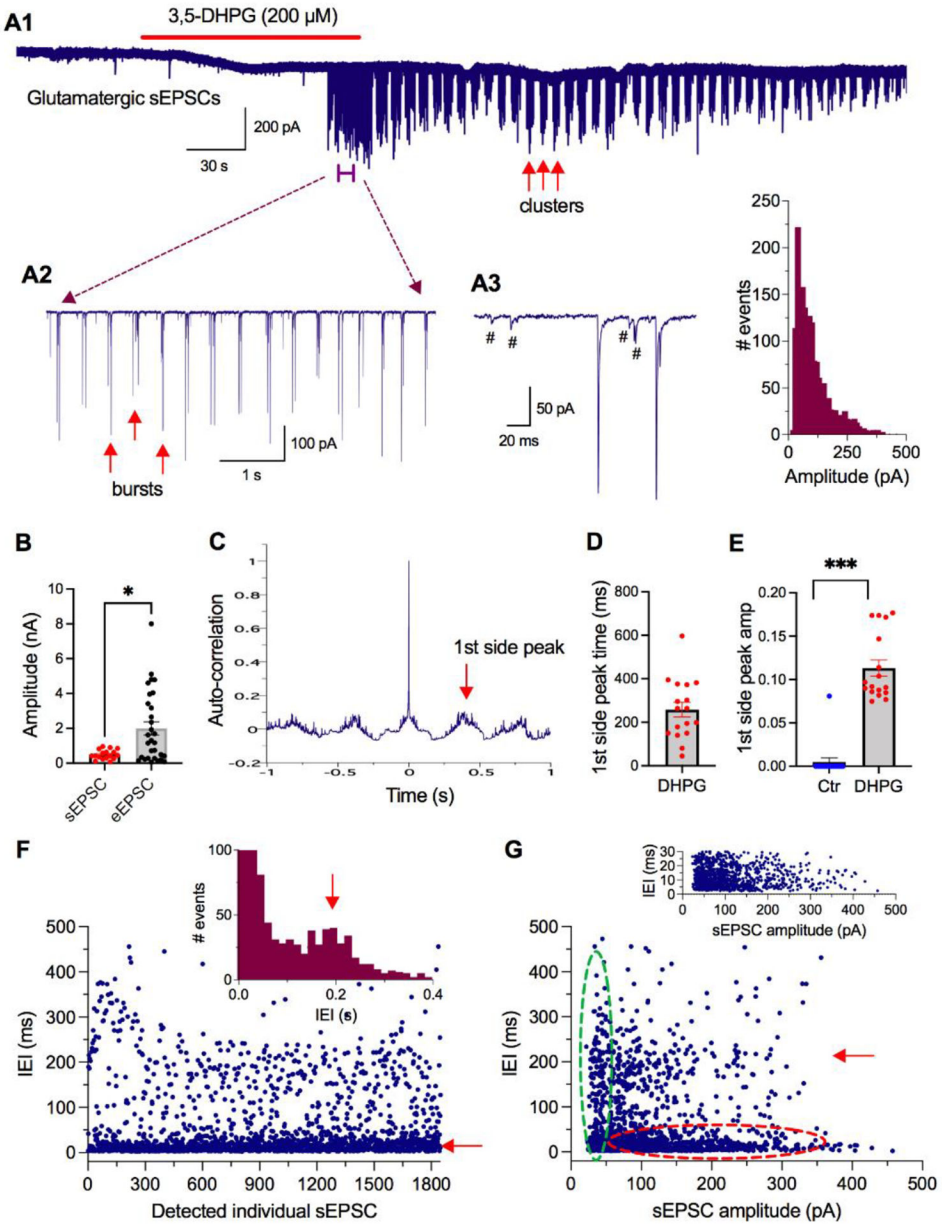

Figure 2.

Activation of mGluR I triggered temporally patterned AP-dependent spontaneous glutamate release onto a subpopulation of MNTB neurons (17 out of 107 cells, 16%), most of which (13 out of 17 cells, 76%) also displayed bursts of sEPSCs. (**A**) Activation of mGluR I by 3,5-DHPG (200 μM) resulted in large sEPSCs forming clusters. The clusters were obvious during the wash of 3,5-DHPG, with a gap of about 5 s between two neighboring clusters (A1). Within each cluster, and during the initial phase of the drug application, bursts (with two or more large sEPSCs) had a relatively constant IEI (A2). The large sEPSCs were interspersed with much smaller sEPSCs (A3, indicated by the symbol #). (**B**) Although apparently larger than the quantal size, the maximal amplitude of sEPSCs under 3,5-DHPG (n=17) was significantly smaller than that of eEPSCs recorded under the same

conditions (n=30; unpaired t test p=0.0269). (**C**) Autocorrelogram detected the first side peak at the timing of 395 ms, which approximates the visually-detected interval between two neighboring bursts. The amplitude of the first side peak was 0.104. (**D**) The timing of the first side peaks of the bursts of sEPSCs (n=17). (**E**) Paired t test detected significant difference in the first peak amplitude between the control and the drug group (n=17). Under control conditions, 16 cells did not have side peaks in their autocorrelograms, and the amplitude was assigned a value of zero. (**F**) When the IEIs were plotted sequentially in the order of event detection, the distribution of the IEIs showed a group of events with very small IEIs (indicated by the red arrow in the main graph), and an apparent group of events with IEI at about 200 ms (indicated by the red arrow in the inset). The histogram distribution of the IEIs showed two peaks, with the first peak averaging at about 15 ms matching the interval between the large sEPSCs within the bursts, and the second peak at about 200 ms. (**G**) Plotting of the IEIs against the amplitudes of sEPSCs. There was one group of sEPSCs that were of the smallest amplitudes (likely quantal size) and varying IEIs (green dashed oval), reflecting the randomness in timing of the quantal release. With increasing amplitudes, a group of large sEPSCs showed a constant IEI of about 15 ms (red dashed oval) matching the interval between large sEPSCs within the bursts, and another group of events at IEI of about 200 ms (red arrow; and the inset) matching half of the timing of the first side peak in the autocorrelogram. Cells were held at −60 mV for EPSC recordings.

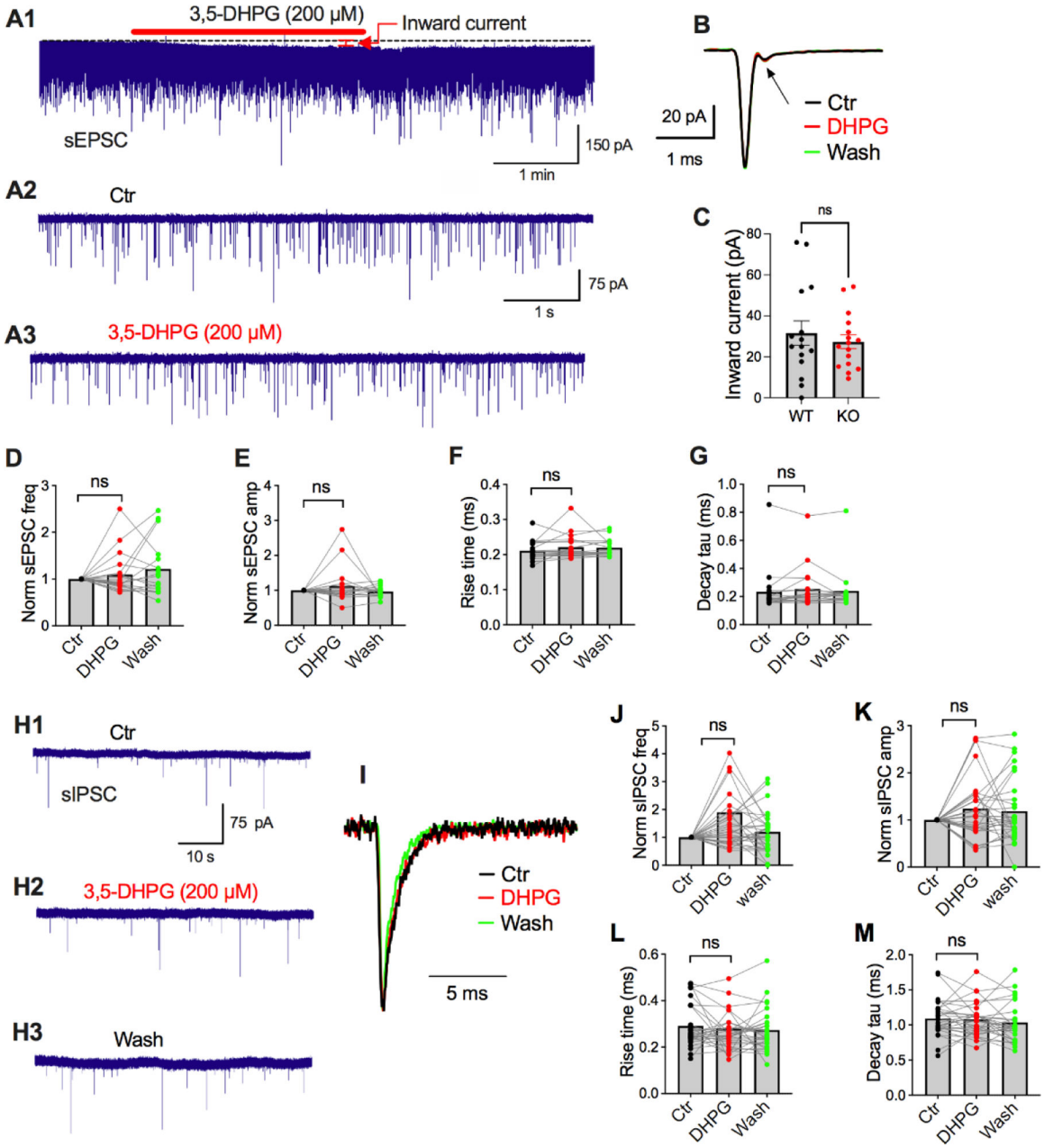

Figure 3.

Knockout of mGluR5 eliminated the enhancement effects of 3,5-DHPG on AP-dependent sEPSCs and sIPSCs of MNTB neurons. All recordings were made from MNTB neurons of mGluR5 KO mice, except for the WT data in panel C. (**A, B**) 3,5-DHPG did not affect sEPSCs of the sample cell. A1 shows the original recording of sEPSCs. Two 7-s segments (A2 and A3) from the control and 3,5-DHPG conditions, respectively, are presented at a larger time scale. Interestingly, a second component (indicated by the arrow in panel B) of the sEPSC was often observed in the recordings from mGluR5 KO mice, which was rarely seen in WT mice (Peng et al., 2020). (**C**) 3,5-DHPG resulted in an inward current, the amplitude of which was not different from that of WT cells, indicating that the current was

primarily mediated by mGluR1, the other member of mGluR I. (**D-G**) We adopted the same protocol as used before (Peng et al., 2020) to detect all the sEPSCs. In population analysis, 3,5-DHPG did not result in significant differences in sEPSC frequency, amplitude, rise time, and decay time constant (n=16). (**H-M**) We adopted the same protocol as used before (Curry et al., 2018) to detect all the sIPSCs. Similarly, 3,5-DHPG did not affect sIPSCs of MNTB neurons in the mGluR5 KO (n=30). The averaged sIPSC traces in panel I were normalized to their peaks.

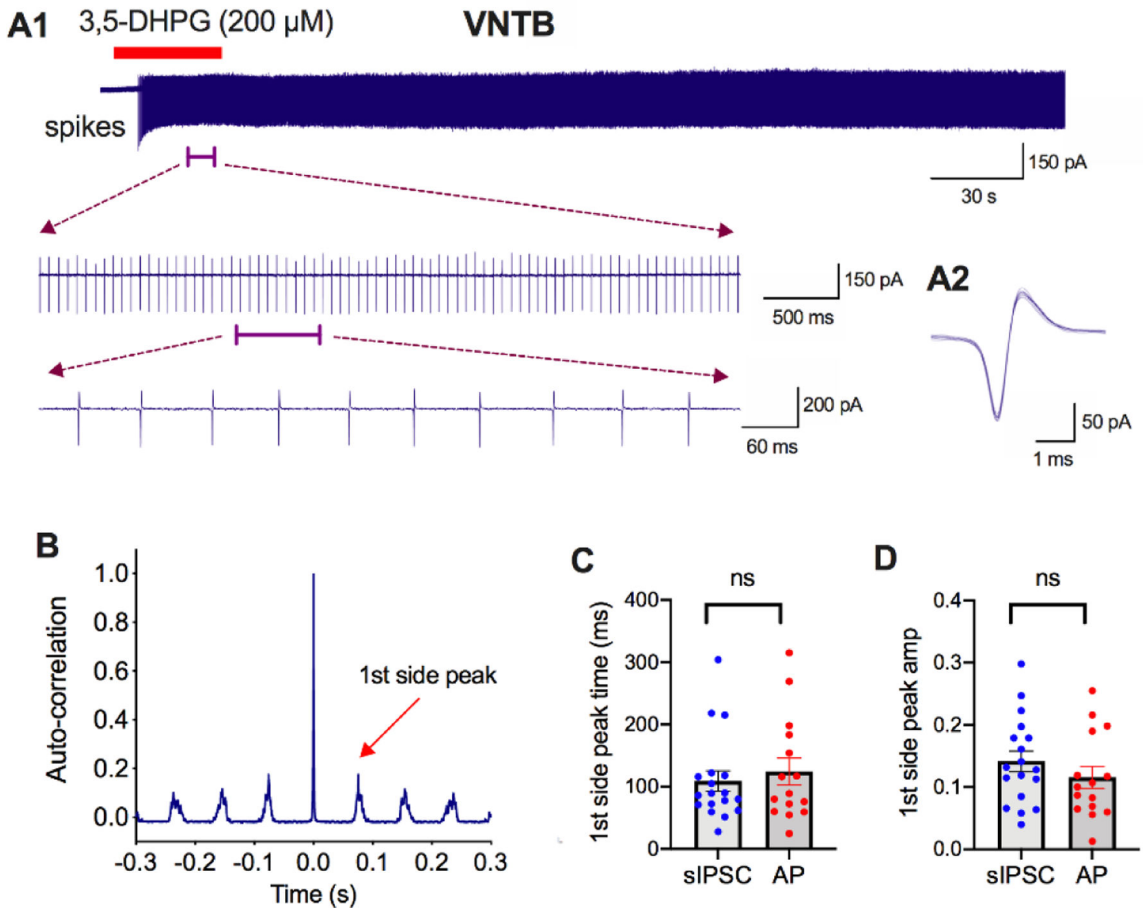

Figure 4.

In response to activation of mGluR I, APs in VNTB neurons had a similar rhythm to that of the large AP-dependent sIPSCs in MNTB neurons. Cell-attached recordings revealed spike generation in a subpopulation of VNTB neurons (16 out of 50 cells, 32%) in response to activation of mGluR I, with 15 cells (30%) displaying rhythmic spike firing. (**A**) Activation of mGluR I by 3,5-DHPG (200 μM) triggered APs with regular IEIs (A1), and the effect was long-lasting. The spikes are of a characteristic bi-phasic waveform for cell-attached extracellular recordings (A2), with relatively uniform amplitudes. (**B**) Autocorrelogram of this sample cell detected the first side peak at the timing of about 85 ms, which approximates the visually detected interval between two neighboring spikes. The amplitude of the first side peak was 0.179. (**C, D**) Average timing and amplitude of the first side peak (n=15) had no significant differences from those for the temporally patterned sIPSCs recorded in MNTB cells (n=18), suggesting a strong correlation of the rhythmic presynaptic firing in VNTB cells and the temporally patterned glycine release in MNTB neurons.

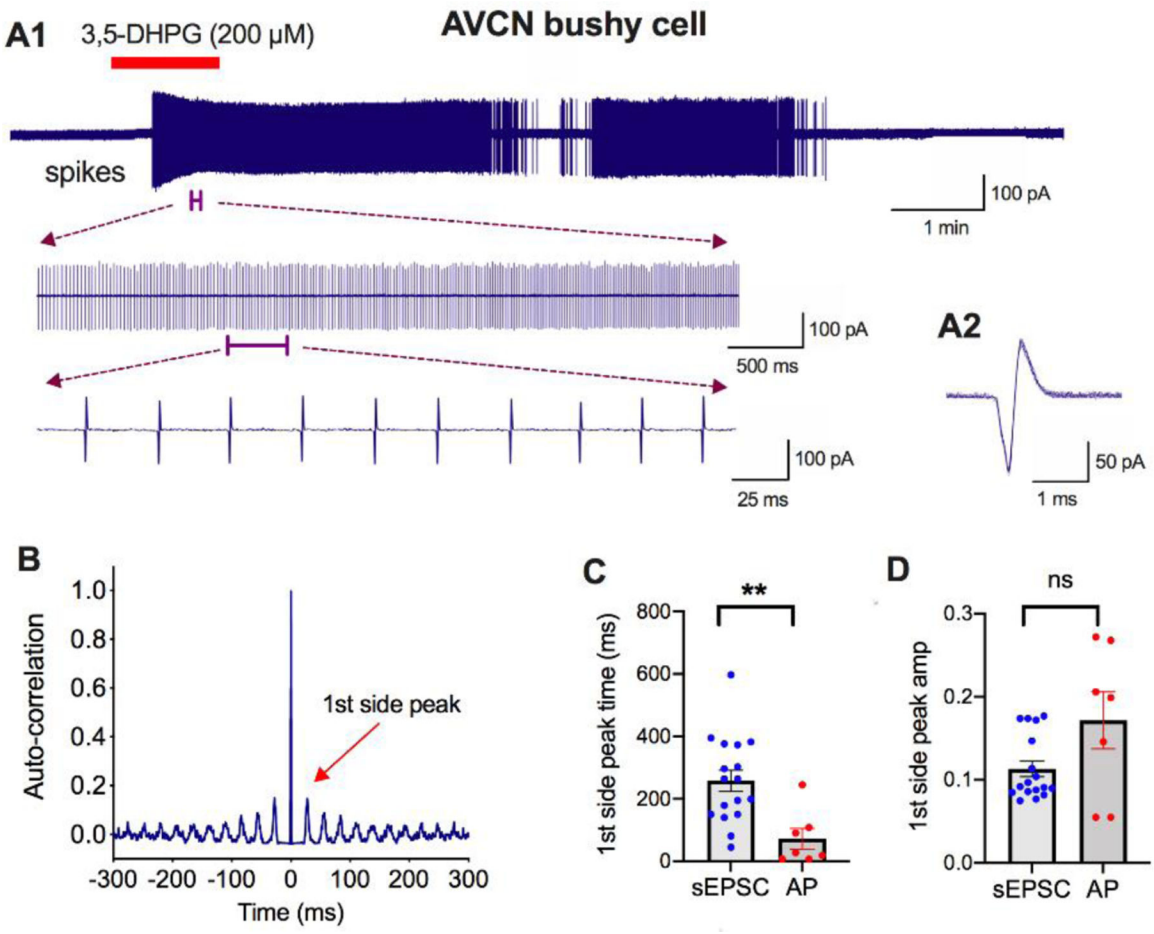

Figure 5.

In response to activation of mGluR I, rhythmogenesis of action potentials in AVCN bushy cells differed in timing from that of the large AP-dependent sEPSCs in MNTB neurons. Cell-attached recordings revealed spike generation in a subpopulation of AVCN bushy cells (12 out of 38 cells, 32%) in response to activation of mGluR I, with 7 cells (18%) displaying rhythmic spike firing. (**A**) Activation of mGluR I by 3,5-DHPG (200 μM) triggered APs with regular IEIs (A1), and the effect was long-lasting (minutes after washout of the drug). The spike waveform is similar to that in VNTB cells (A2). (**B**) Autocorrelogram for a 6-s segment of the recording under 3,5-DHPG detected the first side peak at the timing of about 25 ms, which approximates the visually detected interval between two neighboring spikes. The amplitude of the first side peak was 0.149, representing the strength of the periodicity for temporally patterned spikes. (**C, D**) Average timing of the first side peak of the spikes of the cells with rhythmic spike firing (n=7) was significantly shorter than that of the bursting sEPSCs recorded in MNTB cells (n=17), whereas the average amplitude of the first side peak had no differences.

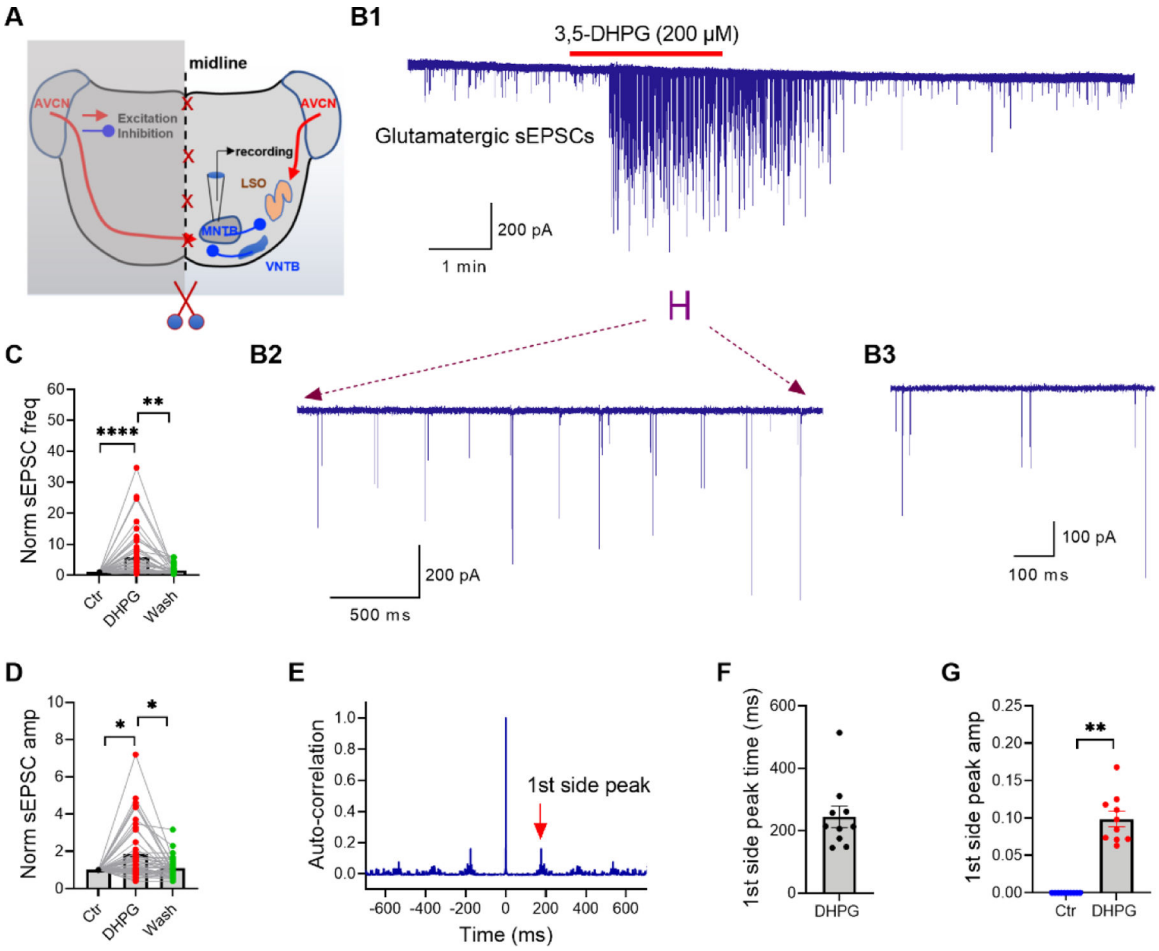

Figure 6.

The effects of mGluR I on sEPSCs of MNTB neurons did not depend on the presence of the cell bodies of neurons in the contralateral AVCN. In half brainstem slices, in which the connection between the contralateral AVCN and the MNTB was completely severed, activation of mGluR I enhanced sEPSCs and triggered temporally patterned AP-dependent spontaneous glutamate release onto a subpopulation of MNTB neurons (10 out of 44 cells, 23%), 8 of which also displayed bursts of sEPSCs. **(A)** Schematic drawing of the half brain slice preparation. **(B)** Effects of bath-applied 3,5-DHPG (200 μM) on sEPSCs in a representative MNTB neuron. **(C, D)** 3,5-DHPG significantly increased the normalized frequency and amplitude of sEPSCs (n=44). **(E)** Autocorrelogram of another cell detected the first side peak at the timing of 178 ms. **(F)** The average of the first side peak time was 244 ms (n=10). **(G)** The amplitude of the first side peak under 3,5-DHPG was significantly larger than that under control condition (n=10), under which none of the cells displayed any rhythmic sEPSCs.

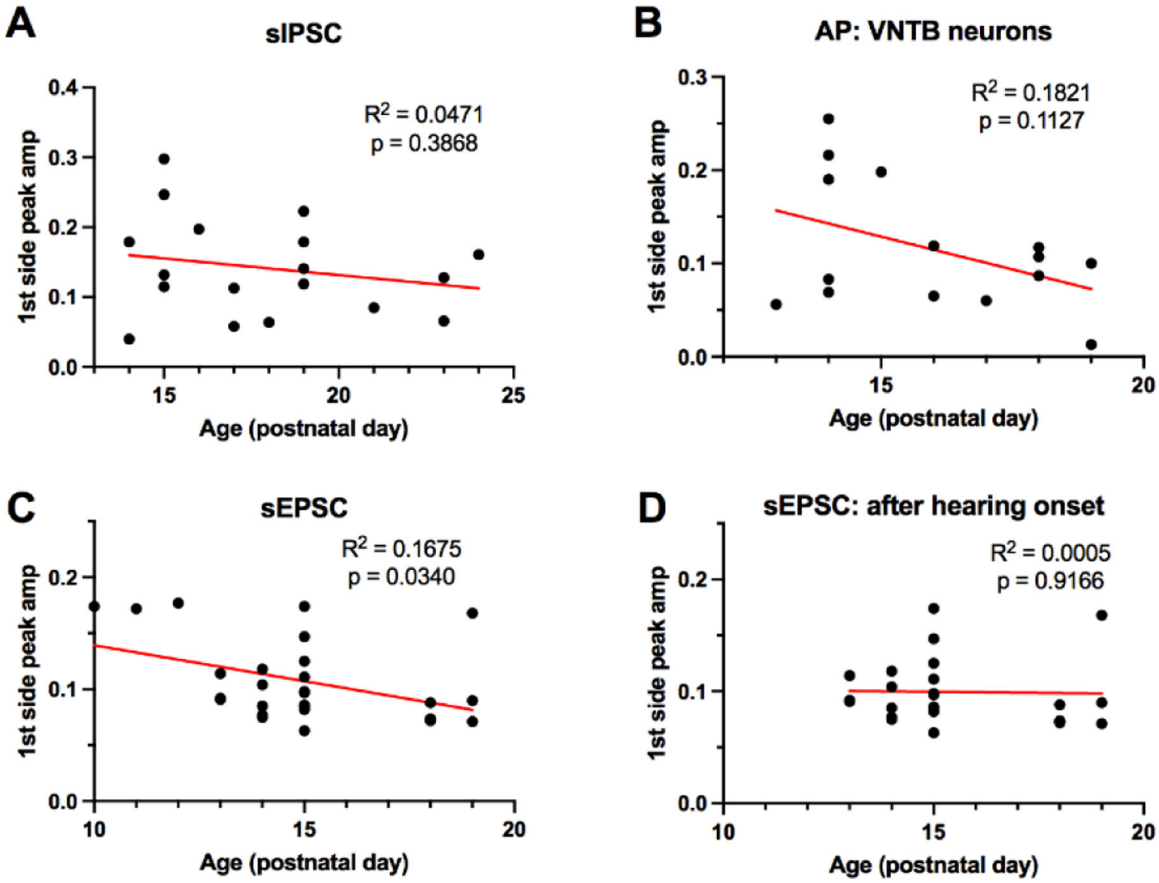

Figure 7.

Age dependence of the auto-correlation strength of rhythmic activities. **(A, B)** No significant correlation was detected between the 1st side peak amplitude of the rhythmic sIPSCs of MNTB neurons and the mouse age (n=18), and between the 1st side peak amplitude of the rhythmic APs of VNTB neurons and the mouse age (n=15), although there seemed to be a trend of a decrease in rhythmic strength with increasing age. **(C)** For rhythmic sEPSCs of MNTB neurons, a significant correlation was detected between the 1st side peak amplitude and the mouse age (n=27). **(D)** However, after excluding the three data points from animals prior to hearing onset, the correlation disappeared (n=24), suggesting a developmental shift in the rhythmic activity after hearing onset.

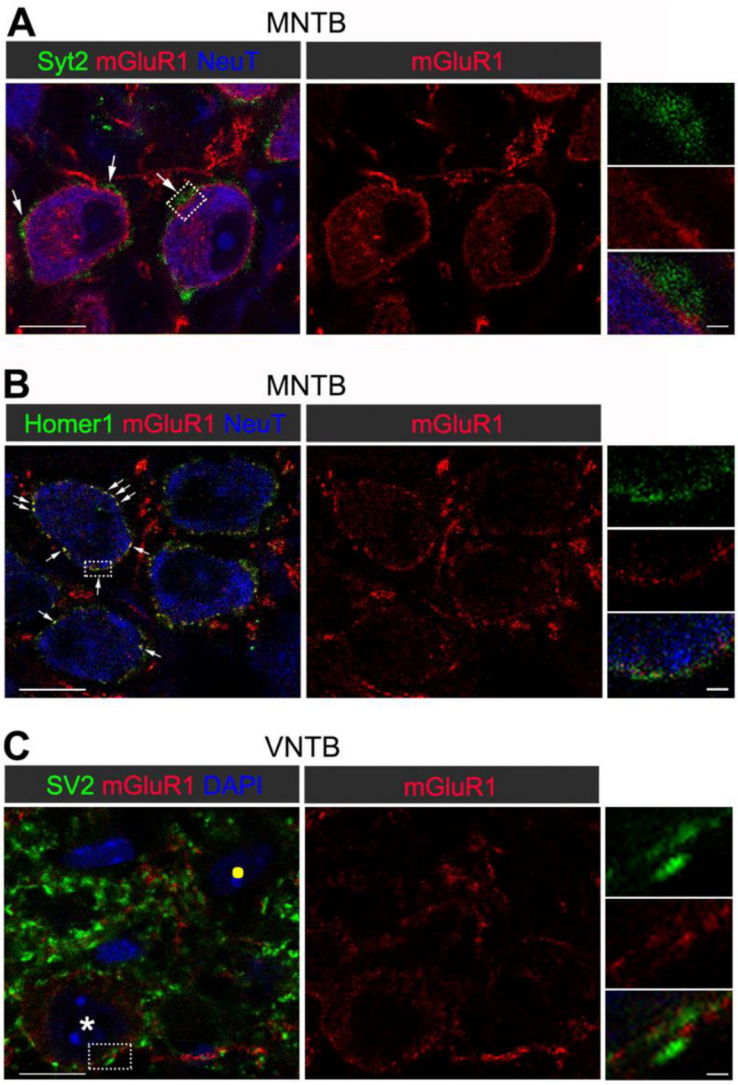

Figure 8.

mGluR1 localization in the cell bodies of VNTB, but not in their axon terminals within MNTB, in P14 wildtype mice. **(A)** Triple immunostaining of mGluR1 (red) and Syt2 (green) in the MNTB with NeuroTrace (NeuT) counterstain (blue). Arrows point out an opposite distribution of Syt2 and mGluR1. A closer view of the region outlined by the white-dotted box is shown in the right column (also applicable to images in B and C). **(B)** Immunostaining of mGluR1 (red) and Homer1 (green) in the MNTB with NeuroTrace (NeuT) counterstain (blue). mGluR1 immunoreactivity encircled MNTB cell bodies and overlapped with Homer1. **(C)** Immunostaining of mGluR1 (red) and SV2 (green) in the VNTB with DAPI counterstain (blue). mGluR1-immunoreactive puncta were opposed to SV2-labeled terminals in VNTB. Somatic mGluR1 was evident in some VNTB neurons (white asterisks). Yellow dot indicates a cell body in the VNTB that did contain mGluR1 puncta. Scale bars = 10 μm in A-C; 1 μm in all magnified images in the right column.

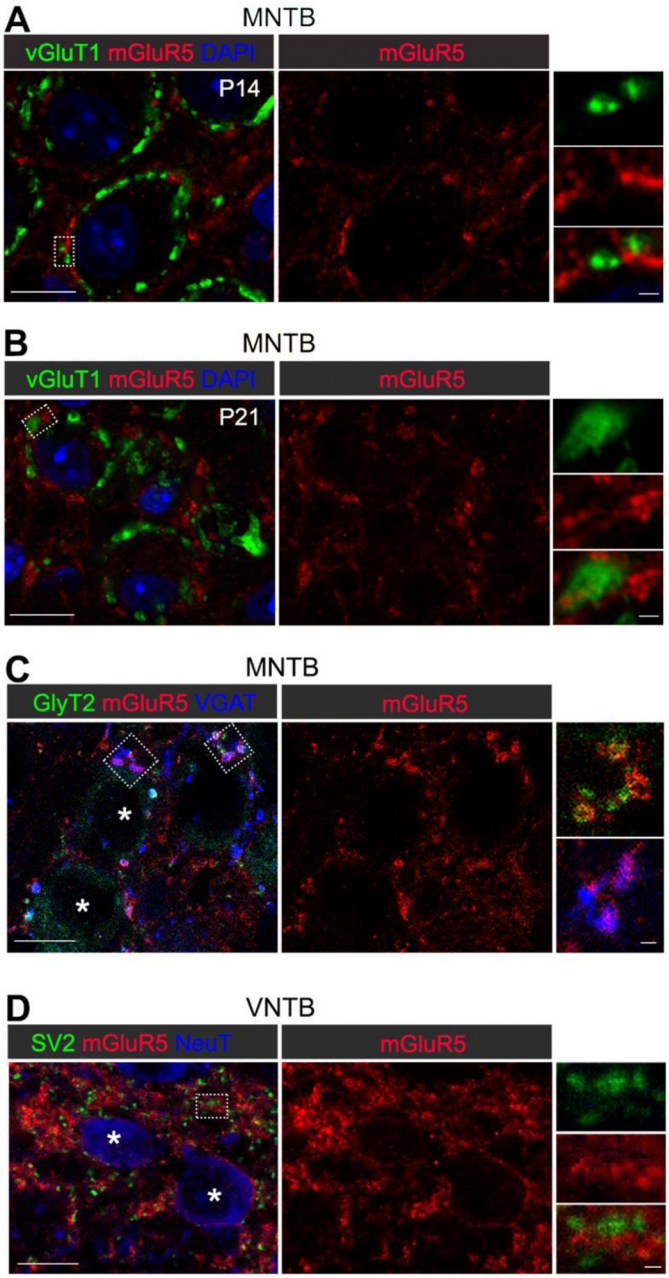

Figure 9.

VNTB neurons contained mGluR5 in their axon terminals within the MNTB but not in their cell bodies, in P14 and P21 wildtype mice. **(A-B)** Triple immunostaining of mGluR5 (red) and vGluT1 (green) in the P14 (A) and P21 (B) MNTB with DAPI counterstain (blue). mGluR5 immunoreactivity was largely non-overlapped with vGluT1-containing terminals. Closer views of the regions outlined by the white-dotted boxes are shown in the right column (also applicable to images in C and D). **(C)** Immunostaining of mGluR5 (red), GlyT2 (green) and VGAT (blue) in the MNTB. mGluR5 immunoreactivity overlapped with GlyT2- and VGAT-labeled terminals. Somatic mGluR5 puncta were evident in the MNTB (asterisks). **(D)** Immunostaining of mGluR5 (red) and SV2 (green) in the VNTB

with NeuroTrace (NeuT) counterstain (blue). Most mGluR5-immunoreactive puncta did not overlap with SV2-labeled terminals in the VNTB. Neuronal cell bodies in VNTB (asterisks) lacked mGluR5. Scale bars = 10 μm in A-C; 1 μm in all magnified images in the right column.

Table 1.

Primary antibodies for immunohistochemistry.

Antibody	Manufacturer, Cat.#	Dilution & concentration	RRID
mGluR1	Cell Signaling Technology, Cat. #12551	1:500 dilution	AB_2797953
mGluR5	Abcam, Cat. #ab76316	1:500 dilution 0.28 μg/ml	AB_1523944
SV2	DSHB, Cat. #SV2	1:1000 dilution 0.51 μg/ml	AB_2315387
Syt2	DSHB, Cat. #Znp-1	1:1000 dilution 0.21 μg/ml	AB_2315626
GlyT2	Synaptic Systems, Cat. #272004	1:500 dilution 0.5 μg/ml	AB_2619998
VGAT	Sigma Aldrich, Cat. #AMAB91043	1:500 dilution	AB_2665778
Homer1	Synaptic Systems, Cat. #160308	1:500 dilution 2 μg/ml	AB_2923010
vGluT1	Abcam, Cat. #242204	1:2000 dilution 0.5 μg/ml	AB_2936821

Note: the concentrations of the antibodies for mGluR1 and VGAT were not available from the manufacturers, although the dilutions and the RRID shall be of sufficient information.

Table 2.

Cell numbers and percentages with temporally patterned sIPSCs and/or bursting sEPSCs, in response to activation of mGluR I by 3,5-DHPG (200 μM), in MNTB neurons of WT and Fmr1 KO mice.

PSC	Genotype (#total cells)	#cells with patterned PSCs (% of total cells)	Chi-square p	#cells with bursting PSCs (% of cells with patterned PSCs)
sIPSC	WT (27)	10 (37%)		0 (0%)
	KO (31)	8 (26%)	0.4041	2 (25%)
sEPSC	WT (95)	15 (16%)		11 (73%)
	KO (12)	2 (17%)	>0.9999	2 (100%)

PSC: postsynaptic current; WT: wildtype; KO: Fmr1 knockout